Science & Technology
Facilities Council

SCARF Annual Report 2010-2011

P Oliver (ed)

November 2011

SCARF Annual Report 2010-2011
Version: 1.5

Date: 07/11/2011

Edited by Peter Oliver (peter.oliver@stfc.ac.uk) 01235 441564
Content written by the respective authors

DATE	REVISION	CHANGES
07/11/11	1.2-1.5	Added SCARF developments and more scientific content.
03/08/11	1.1	Scientific Content Added for 2010-11
15/07/11	1.0	Initial document

Abstract

Annual Report on the Usage and Scientific Impact of the SCARF Service

Dissemination

The is a public document

Contents

1.   SCARF SERVICE

SCARF is a High Performance Cluster for STFC staff, Facilities (ISIS, DIAMOND, CLF) and their users. The SCARF Service was started in 2004 and has been upgraded year on year and now represents a significant capital investment in High Performance Computing. Overall SCARF now has over 2400 CPU cores, 5TB memory and 100TB of diskspace (Details in Appendix 1). This report covers the year 2010-11 and outlines the research that SCARF has enabled.

1.1   SCARF Usage by Department

Each time a researcher uses the SCARF service the CPU time used is recorded. In total over 6.1M CPU hours were used on SCARF during 2010-11.
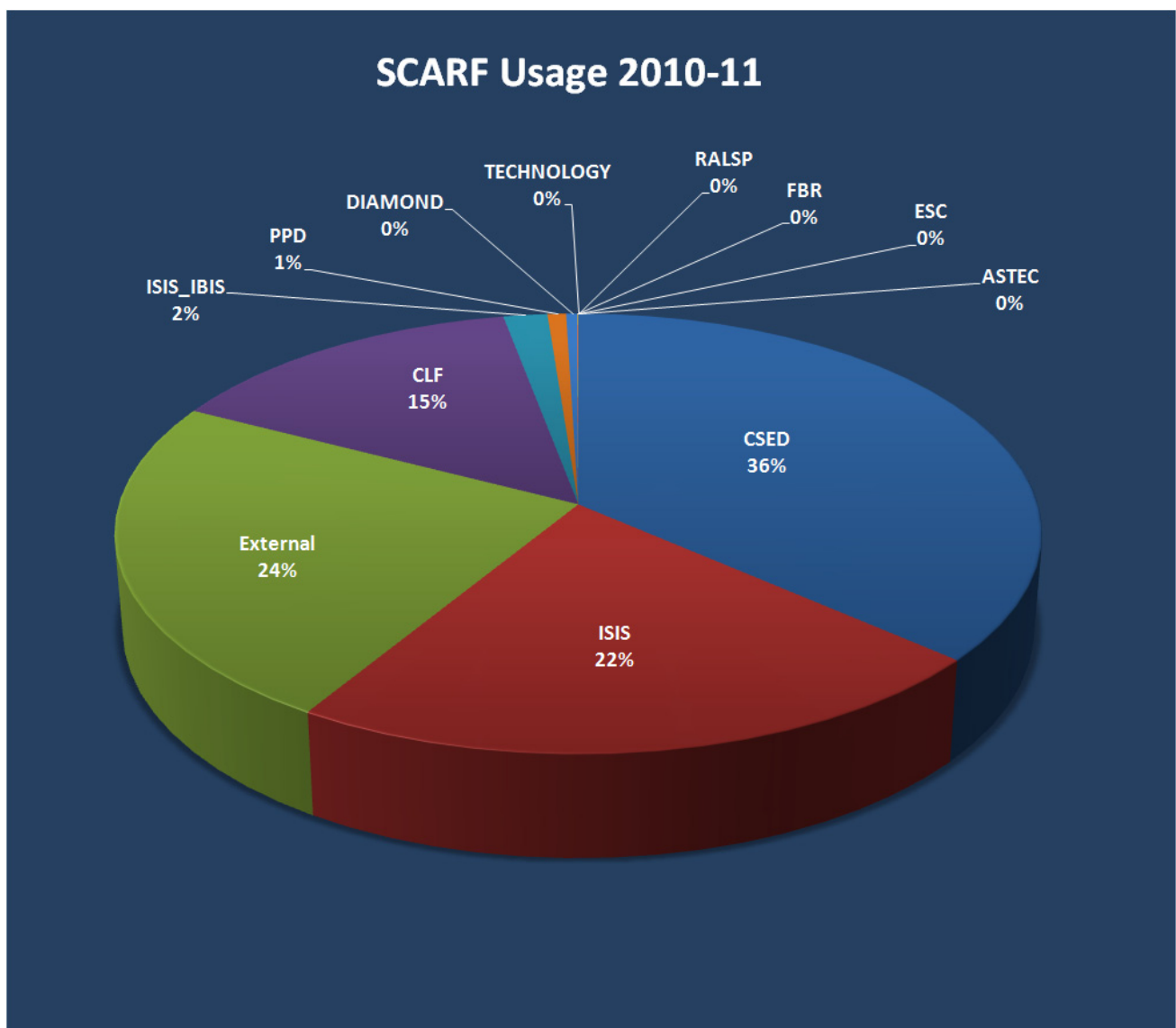
Figure 1: Pie chart showing percentage usage of the SCARF service by department

It is clear from the usage chart that ISIS and CSE are the largest users of SCARF. The External Use category measures the usage from STFC collaborations with Glasgow University, Imperial College, Oxford University and Queens University Belfast.

Dept		2010			2009	
	Active Users	CPU hrs	%	Active Users	CPU hrs	%
CSE	17	2194047.5	35.9	13	2635127.2	43.1
ISIS	19	1357940.5	22.2	12	1272635.2	20.8
External	7	1471784.9	24.1	7	856648.8	14.0
CLF	7	908121.6	14.9	3	392931.1	6.4
ISIS_IBIS	5	104702.8	1.7	4	258576.5	4.2
PPD	1	44299.4	0.7	1	338.4	0.0
DIAMOND	3	26503.5	0.4	1	2433.4	0.0
FBR	1	587.3	0.0	1	25.5	0.0
ESC	7	244.5	0.0	9	25978.5	0.4
ASTEC	2	0.6	0.0	2	26035.7	0.4
RALSP	1	2.2	0.0	1	7.1	0.0
TECHNOLOGY	1	1577.2	0.0	1	0.0	0.0
Totals	71	6109811.8	100.0	55	5470737.5	

Figure 2: Table displaying detailed usage from 2010-11 comparing with 2009-10

A significant amount of computational resource has been used on SCARF, section 3 highlights some of the scientific achievements that have been enabled.

1.2   SCARF Availability

The availability of SCARF is given in the figure below. This availability measures when users could login to SCARF and submit jobs . SCARF achieved 100.0% availability during 2010-11
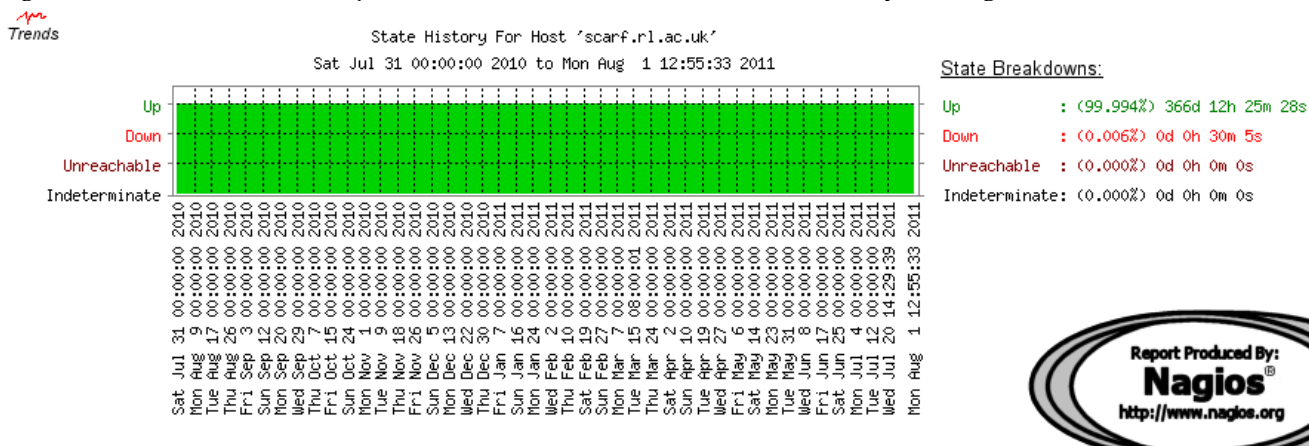
Figure 3: Availability for SCARF

The table below details the availability of compute nodes by purchase date. It is evident that the older equipment purchased in 2006 is giving the most problems. This supports the rolling upgrade of SCARF and the 2006 equipment will be phased out for general use in 2011-12.

Year Purchased	Compute node Availability 2009-10	Compute node Availability 2010-11
2006	94.2%	94.28%
2007	98.5%	99.38%
2008	99.2%	98.62%
2009	98.4%	99.79%
2010	98.8%	99.72%
2011	NA	100.00%

Figure 4: Availability vs Year Purchased

1.3 SCARF Developments 2010-11

- Major SCARF Developments are listed below. A more detailed list can be found in Appendix 5
  - Major upgrade to RedHat 5, LSF 8 and MPI 8
  - New capacity added
    - 384 Intel X5660 CPU cores for general use went into production in May 2011

1.4 Future Development

- SCARF 2012 Hardware Upgrade
  - ~300 CPU Cores for General Use
- Upgrade to parallel filesystem for /SCRATCH
  - Faster and more capacity

1.5 Help and Support

For any queries concerning the SCARF service please email the SCARF Helpdesk;
scarf@hpc-support.rl.ac.uk

2.   PUBLICATIONS AND PRESENTATIONS

2.1   Publications

A list of publications is given in Appendix 3. A way of estimating the impact that SCARF has had is to analyse the Journal Impact Factor using the Journal Citation Reports published by Thomson Reuters. The average Impact Factor for Journals published as a result of using SCARF is 3.6. This compares to an average impact factor across all 6600 journals of 2.2. This is a simplistic analysis but demonstrates that the science done on SCARF is having a significant impact.

2.2   Presentations

Scientists have presented their work at 10 international conferences (Appendix 3). This helps to demonstrate that the science enabled by SCARF is world class.

3.   SCIENCE HIGHLIGHTS

3.1   R.M.G.M. Trines,[1] F. Fiúza,[2] R. Bingham,[1] R.A. Fonseca,[2] L.O. Silva,[2] R.A. Cairns,[3] and P.A. Norreys[1] (CLF)

[1]*Central Laser Facility, STFC Rutherford Appleton Laboratory, Didcot, Oxon, OX11 0QX, United Kingdom*
[2]*GoLP/Instituto de Plasmas e Fusão Nuclear - Laboratorio Associado, Instituto Superior Técnico, 1049-001 Lisbon, Portugal*
[3]*University of St Andrews, St Andrews, Fife KY16 9AJ, United Kingdom*

3.1.1   *Production of picosecond, kilojoule, petawatt laser pulses via Raman amplification of nanosecond pulses*

Raman amplification in plasma has been promoted as a means of compressing picosecond optical laser pulses to femtosecond duration to explore the intensity frontier. Here we show for the first time that it can be used, with equal success, to compress laser pulses from nanosecond to picosecond duration. Simulations show up to 60% energy transfer from pump to probe pulses, implying that multi-kilojoule ultra-violet petawatt laser pulses can be produced using this scheme. This has important consequences for the demonstration of fast-ignition inertial confinement fusion. Previous studies of Raman amplification have concentrated on reaching the intensity frontier, which requires ultra-short pulses in the femtosecond regime [1-7]. Here we present novel particle-in-cell simulations, supported by analytic theory, that confirm that Raman amplification of high-energy nanosecond pulses in plasma can generate efficient petawatt peak power pulses of picosecond duration with high conversion efficiency (up to 60%). The scheme can easily be scaled from ω_0 to $3\omega_0$ pulses: only the plasma density needs to be adjusted such that the ratio ω_0/ω_P remains fixed.

This scheme provides a new route to explore the full parameter space for the realisation of the fast ignition inertial confinement fusion concept in the laboratory, as this requires pulses of picosecond duration and multi-petawatt power [8-13]. This work also opens up a wide range of other high energy density physics research applications, including monochromatic K_α x-ray [14], proton beam [15] and Compton radiography of dense plasmas [16], among many others.
Raman amplification of ultra-short (~25 fs) pulses at high intensities was the subject of an extensive recent investigation [6]. It follows from the self-similar theory of Raman amplification developed by Malkin, Shvets and Fisch [2] that ns-to-ps compression can be accomplished by reducing the

intensities of pump and probe. If one fixes $\omega_0/\omega_P = 20$ and $t_{pump}/t_{probe} = 1000$, as in [6], then the pump intensity needed to obtain a certain optimal probe duration is given by:

$$I_{pump} = 3.9 \times 10^{11} / (t_{probe}[ps])^2 [W/cm^2]$$

independent of pump laser wave length. As an example, producing a 2 ps probe from a 2 ns pump requires an intensity of 1.0×10^{11} W/cm^2.

	I	II	III	III′	IV	V	VI
a0	0.0044	0.003	0.0016	0.0016	0.001	0.001	0.00056
a1	0.0044	0.003	0.0044	0.0044	0.003	0.003	0.00056
t_{pump} (ps)	100	133	100	100	67	133	133
t_{probe} (fs)	65	28	230	330	400	283	2180
Eff. (%)	20	39	50	40	60	44	7

Table I: Summary of our simulation results. In each simulation, $\lambda_0 = 351$ nm and $\omega_0/\omega_p = 20$ were used. For each simulation, the initial pump (a_0) and probe (a_1) amplitudes, initial pump (t_{pump}) and final probe (t_{probe}) duration, and energy transfer efficiency are given. Simulation (III′) is similar to (III), only using mobile ions (all others use static ions).

This has been explored in a series of full particle-in-cell (PIC) numerical simulations using the codes XOOPIC [17] and OSIRIS [18]. These simulations were performed on the Scarf-Lexicon Cluster (STFC RAL), the IST Cluster (IST Lisbon), the Hoffman cluster (UCLA) and the Jugene supercomputer (Germany). The summary of our simulation results is shown in Table I. Overall, the final probe duration is found to increase with decreasing pump amplitude, and to decrease with increasing pump duration, confirming our initial hypothesis. The poor efficiency in (I) is caused by the combination of high pump intensity and long interaction length, triggering premature pump RBS and probe saturation. The poor efficiency in (VI) is caused by the long start-up time (see below) resulting from the low pump and probe intensities.
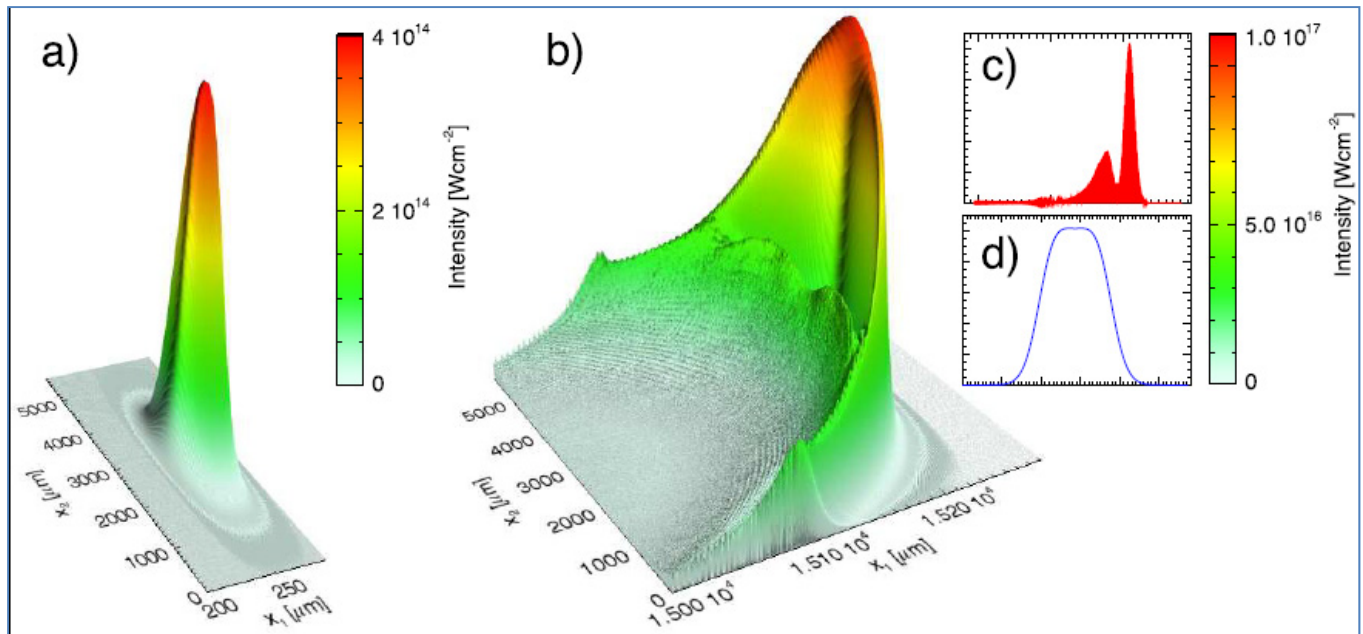
Figure 5: Raman amplification of a 100 ps long pump to obtain a ~150 fs, mm wide, 2 PW probe, for a wave length of 351 nm. (a) Initial and (b) final intensity profile of the probe pulse after amplification in a 1.5 cm plasma column. Insets show central lineouts of the amplified pulse in the (c) longitudinal and (d) transverse directions.

In order to study the stability of the process in multiple dimensions, where transverse instabilities can come into play, we have performed a 2D OSIRIS simulation using the parameters of simulation (III) and a probe spot FWHM of 1.2 mm. This relatively wide probe pulse is efficiently amplified to a peak intensity of 10^{17} Wcm^{-2}, corresponding to a final power of 2 PW (Figure 5). For these optimized parameters, and due to the relatively low pump intensity, transverse instabilities are controlled and the amplified pulse retains a smooth envelope.

In summary, we have investigated the Raman amplification and compression of nanosecond laser pulses to picosecond duration, exploiting the self-similar properties of the process. We have shown that, for a constant pump-to-probe compression ratio, the optimal pump and probe durations will increase for decreasing pump intensity, allowing the production of picoseconds pulses of moderate intensity but large total energy. Energy transfer efficiencies of up to 60% have been found. This approach provides a potential route to the full-scale demonstration of fast ignition inertial confinement fusion using existing facilities.

1. G. Shvets et al., Phys. Rev. Lett. 81, 4879-4882 (1998).
2. V.M. Malkin et al., Phys. Rev. Lett. 82, 4448-4451 (1999).
3. V.M. Malkin and N.J. Fisch, Phys. Plasmas 12, 044507 (2005).
4. J. Ren et al., Nature Physics 3, 732-736 (2007).
5. Y. Ping et al., Phys. Plasmas 16, 123113 (2009).
6. R.M.G.M. Trines et al., Nature Physics 7, 87 (2011).
7. R.K. Kirkwood et al., Phys. Plasmas 18, 056311 (2011).
8. S. Atzeni et al., Phys. Plasmas 15, 056311 (2008).
9. J. Honrubia and J. Meyer-ter-Vehn, Plasma Phys. Control. Fusion 51 014008 (2009).
10. A.J. Kemp, Y. Sentoku and M. Tabak, Phys. Rev. E 79, 066406 (2009).
11. P.A. Norreys et al., Nucl. Fusion 49, 104023 (2009).
12. M.S. Wei et al., Phys. Plasmas 15, 083101 (2008).
13. M. Tabak et al., Phys. Plasmas, 1, 1626 (1994).
14. H.-S. Park et al., Phys. Plasmas 13, 056309 (2006).
15. M. Borghesi et al., Phys. Plasmas 9, 2214 (2002).
16. R. Tommasini et al., Rev. Sci. Instrum. 79, 10E901 (2008).
17. J.P. Verboncoeur, A.B. Langdon and N.T. Gladd, Comp. Phys. Comm. 87, 199-211 (1995).
18. R.A. Fonseca, L.O. Silva, R.G. Hemker, et al., Lect. Not. Comp. Sci. 2331, 342-351 (2002).

3.2   Adam Dobbs (Imperial College London, ISIS Collaboration)

3.2.1   ORBIT Simulations of ISIS Beam Loss Induced by the MICE Target

The Muon Ionisation Cooling Experiment (MICE) is a proof-of-principle experiment designed to demonstrate muon ionisation cooling, for application to a future Neutrino Factory or Muon Collider, for the rst time. MICE is housed at the Rutherford Appleton Laboratory and uses the Lab's 800 MeV ISIS synchrotron as a proton driver. In order to generate particles for the MICE Muon Beamline a cylindrical titanium target is pulsed into the ISIS beam. The hadronic interactions between the proton beam and the target nuclei generate a pion shower which is captured by a quadrupole triplet. Subsequent decay of these pions produces the desired muons.

An additional effect of the MICE target is to increase the beam loss levels present in ISIS. This can disrupt beam for other ISIS users or make hands on maintenance more difficult due to increased activation levels. As such, it is important that this effect is understood in order to help maximise MICE particle rate while causing a minimum of disruption to ISIS running. ORBIT (Objective Ring Beam Injection and Tracking) simulations, running on the STFC SCARF cluster, are used to help understand the induced beam loss distribution patterns around ISIS and how altering the MICE target parameters (material, geometry, etc.) affects them.

Simulation results indicate that losses due to the MICE target are split between losses located near to the target itself and losses near to the ISIS collimator system. Increasing the atomic number of the target material causes the ratio of losses at these positions to swing more towards losses at the target rather than at the collimator system. The target geometry is also observed to affect this ratio. Targets which present a long length of material in the longitudinal direction to the beam tend to have a higher ratio of losses at the target, compared with geometries that present a traversally wide target which is longitudinally thin. The actual cylindrical MICE target produces results in between these two extremes, with simulation indicating that the ratio of losses at the target and at the collimators is approximately 2:1 in this case.

For more details see "Particle rate and host accelerator beam loss on the MICE experiment", A. Dobbs, http://www.hep.ph.ic.ac.uk/~adobbs/Docs/adobbs_thesis.pdf"
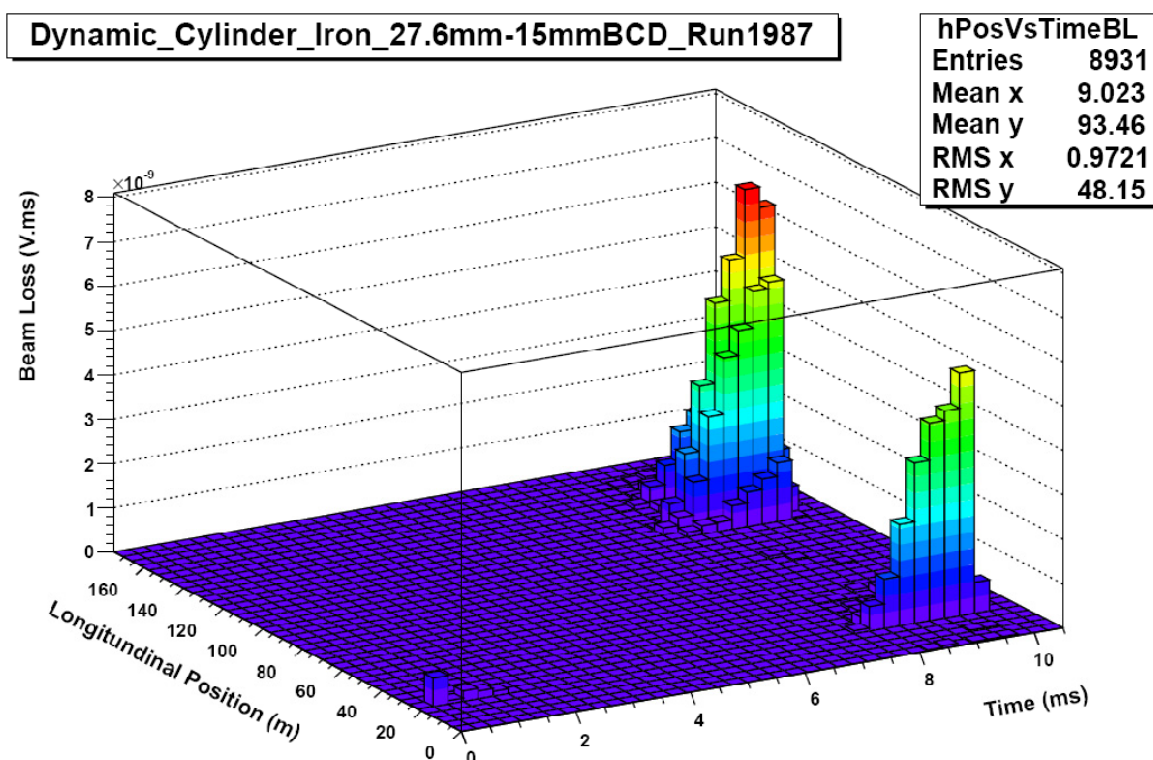
Figure 6: 2D histogram of beam loss as a function of position around the ISIS ring and time in the ISIS cycle in the presence of the MICE target with beam centre distance of 17.6mm.

3.3   Daniel Jones (ISIS)

3.3.1   *Development of a Linear Scaling Divide and Conquer Algorithm for the CRYSTAL Electronic Structure Program.*

Since September 2010, I have been using SCARF as a testing platform for the development of a new linear scaling algorithm for the CRYSTAL electronic structure code. The SCARF cluster has allowed me to perform proof of principle computations to show that the electron density within a relatively small diamond cluster is nearly identical to that of a diamond crystal. I have also used SCARF to perform tests comparing the new divide and conquer algorithm to the more traditional cubic scaling algorithms present in CRYSTAL. CRYSTAL is unique in its ability to perform all electron calculations for very large systems either non-periodic or periodic in 1, 2 or 3 dimensions. The successful development of this algorithm will enable the study of much larger, lower symmetry systems and should be especially suited to biological systems and to molecular crystals.
In addition to this main work, I have performed a few calculations investigating the electronic structure of gallium ferrite ($GaFeO_3$). This work, in collaboration with Prof. Bob Cernek at Manchester University, will attempt to investigate the reason doped $GaFeO_3$ behaves as a multiferroic material.
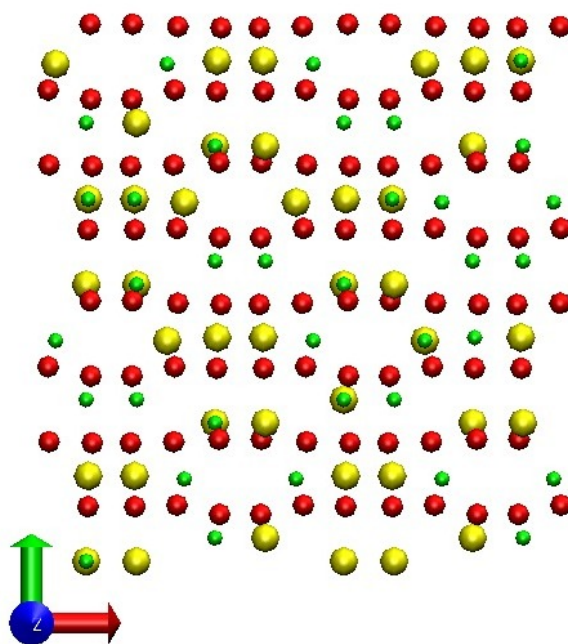
Figure 7: Structure of gallium ferrite (GaFeO3)

Both of these studies are relatively new and, as yet, have not resulted in any publications. I am optimistic that publishable results will be collected by the winter, to be prepared for publication in January-February 2012. I am scheduled to present these findings at MSSC 2011 in Turin, Italy and I have been invited to give a seminar in the autumn term at The University of Warwick.

3.4 Tony Bell (Oxford University, CLF Collaboration)

3.4.1 *Vlasov-Fokker-Planck simulations of laboratory and astrophysical plasmas*

Vlasov-Fokker-Planck (VFP) codes are used in plasma physics to model the evolution in space and time of the distribution function of energetic particles under the influence of collisions and electric and magnetic field. In the KALOS formalism, anisotropies in the particle distribution function are described by an expansion in spherical harmonics. This has been widely used to simulate electron transport in laser-produced plasmas. Recently we have coupled a KALOS VFP code to a fluid code to facilitate self-consistent calculations of transport and hydrodynamics. Bell & Tzoufras (2011) used the code to simulate Inertial Fusion Energy. We show that for a suitable choice of laser intensity and laser pulse duration pressures of nearly a Gbar can be generated at solid density. In the shock ignition route to commercial fusion energy production, the high pressure is used to drive a spherically convergent shock into an already compressed fusion target, igniting the target and producing thermonuclear energy. The maximum pressure available to drive the shock is determined by electron transport. Our VFP simulations show that at high laser intensity, long mean free path electrons propagate far into the target, and spread the energy over a large volume. This reduces the peak pressure but it has the positive benefit of delivering the energy to the dense plasma where the thermonuclear ignition hot-spot is formed. The figure shows one quadrant of a target irradiated at the pole as simulated in 2D with fixed hydro. Crucially, energetic electron transport carries energy around the surface of the target to produce a pressure which is much more uniform than the very non-uniform laser irradiation. This smoothing considerably relaxes

constraints on laser geometry. As shown in the figure below , the Spitzer theory for electron heat flow dramatically breaks down under these circumstances.
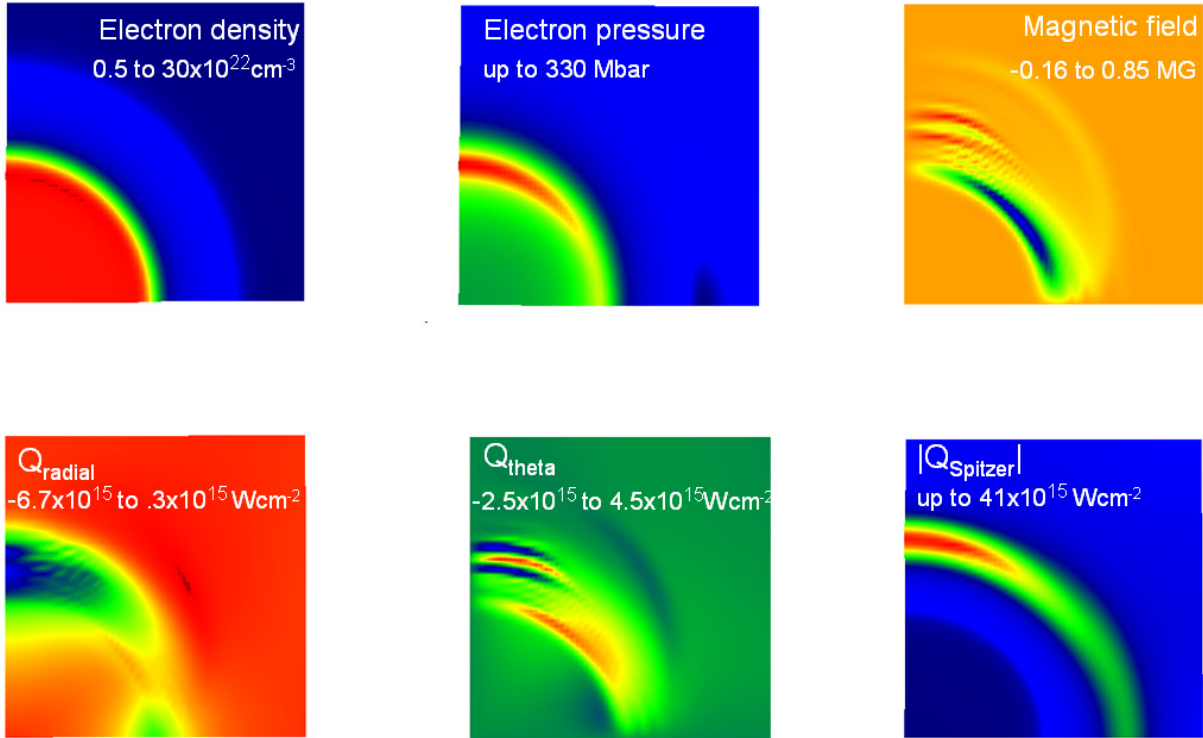

Figure 8: Sections through a solid target irradiated at the pole for 28psec by a laser at an intensity of 8x10^{15}Wcm^{-2}. Top row: electron density, pressure, magnetic field. Bottom row: energy flux radial to the target, energy flux around the surface of the target, the energy flux given by the Spitzer conductivity if it were to apply.

The same VFP-hydro simulation technique can be applied to astrophysical shocks and the acceleration of cosmic rays to PeV energies (Bell, Schure & Reville 2011). The problem is very similar to laser-plasma problems except that the energetic electrons are replaced by energetic cosmic ray protons. There is a similar self-consistent feedback between the propagation of energetic charged particles (electrons or cosmic ray protons), the motion of the magnetised thermal background plasma and amplification of magnetic field which is frozen into the background plasma. We have shown that high-order particle anisotropies have a large effect on the accelerated cosmic ray energy spectrum when the magnetic field is predominantly perpendicular to the shock normal. The power law spectral index is steepened at high velocity shocks. This agrees with observations of supernova remnants. Young rapidly expanding remnants display steeper synchrotron spectra than old slowly expanding remnants. It may also explain why the spectrum of cosmic rays arriving at the earth is steeper than can be accounted for with the standard theory.

3.5 Gabriella Graziano (University College of London and ISIS), Jiří Klimeš (University College of London), Felix Fernandez-Alonso (ISIS), Angelos Michaelides (University College of London)

3.5.1 Soft Nanostructured Materials for Hydrogen Storage

We are using the SCARF cluster to find improved DFT-based descriptions of the adsorption of molecular hydrogen by soft nanostructured materials. In the absence of doping, hydrogen adsorption on light-atom substrates such as graphite and carbon nanotubes is dominated by weak van-der-Waals interactions, posing a challenge to well-established DFT methods. The optB88-vdW functional recently introduced by Klimeš et al. [1] has been designed to circumvent these difficulties. We have already tested this functional on bulk graphite and hexagonal boron nitride, and find a very good agreement with available experimental data [2].

DFT calculations have been carried out on SCARF using the plane-wave code VASP 5.2 and the optB88-vdW exchange-correlation functional with PBE-optimized projector-augmented-wave (PAW) potentials. These calculations show that the optB88-vdW functional provides a satisfactory description of the interaction of hydrogen with graphene, as illustrated the figure below:
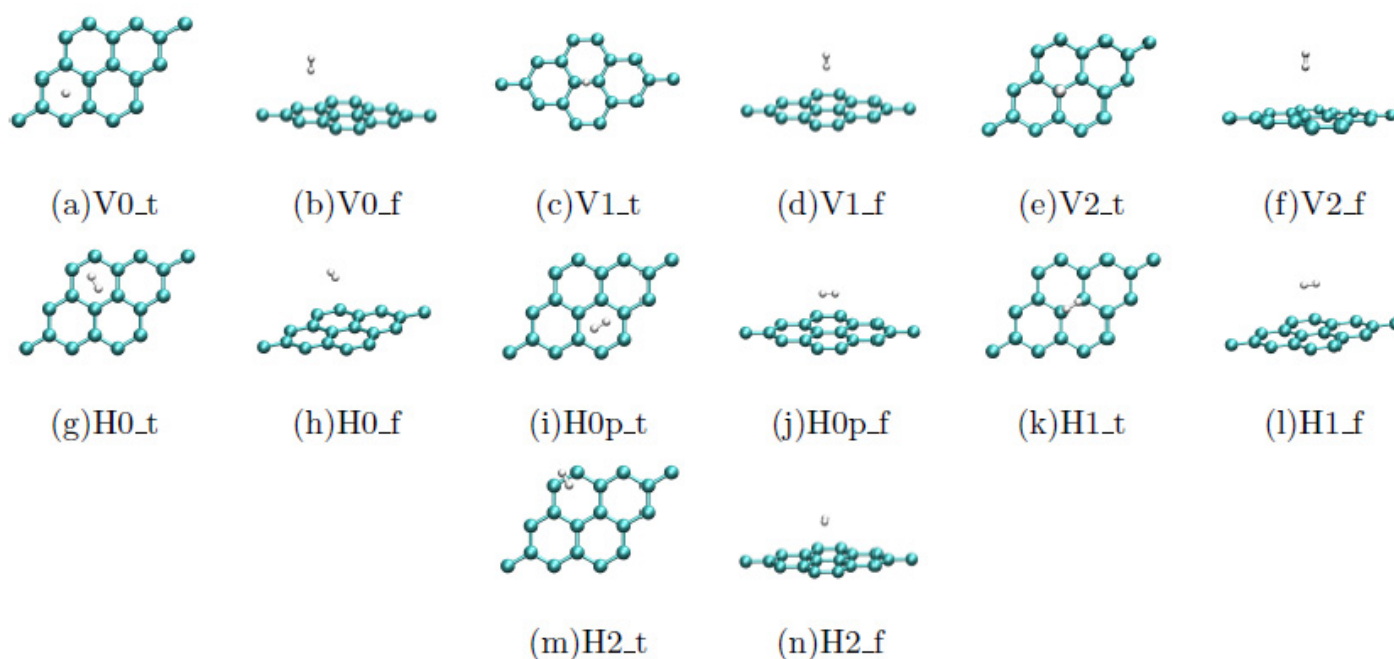

Figure 9: Hydrogen-graphene configurations computed on SCARF. The first row shows different positions of a vertically aligned hydrogen molecule. In the remaining rows, hydrogen is parallel to the grapheme sheets. V(H) refers to configurations where molecular hydrogen is arranged vertically(horizontally) with respect to the surface. For each configuration, top (t) and front (f) views are also shown

Following these benchmark calculations, this new DFT functional will be used to explore the adsorption of molecular hydrogen by layered materials of technological interest.

1. J. Klimeš, D. R. Bowler, and A. Michaelides, J. Phys.: Condens. Matter 22, 022201 (2010).	2. G. Graziano, J. Klimeš, A. Michaelides, and F. Fernandez-Alonso, in preparation.

3.6 Felix Fernandez-Alonso (ISIS) and Matthew Krzystyniak (Nottingham Trent University)

3.6.1 *Hydrogen Dynamics in Condensed Matter: Linking Neutron Data to First-principles Predictions*

In the period 01/08/10 to 01/08/11, we have used the SCARF cluster in research projects aimed at linking first-principles calculations to neutron-scattering experiments carried out at the ISIS Pulsed Neutron and Muon Source, Rutherford Appleton Laboratory. Here, the main goal has been to employ materials modelling software packages available on SCARF to develop new methodologies for a direct comparison between ab initio calculations and spectroscopic studies using neutron Compton (NCS), inelastic (INS), and quasielastic neutron scattering (QENS). Emphasis has been placed on hydrogen-containing materials of fundamental and technological interest. We have developed software tools in Matlab to process and link the output of modelling packages such as CASTEP and Gaussian 09 with observables directly measured in neutron spectroscopy. The following methodology was followed:

1. Calculation of total and projected vibrational densities of states (VDOS) using linear response theory or finite-displacement methods.
2. Matlab-based routines to perform multiple tasks, including: input parsing from the output of ab initio programs, the calculation of relevant observables (e.g., second moments of the nuclear momentum distribution and the Laplacian of the effective Born-Oppenheimer potential), and simulation of neutron data.

The methodology for the calculation of first-principles predictions of the Laplacian of the effective single-particle Born-Oppenheimer potential has been established for the first time. Ab initio calculation of the Laplacian also serves as a tool to calculate the magnitude of final-states effects in NCS, of importance in the design and interpretation of neutron experiments. This newly established methodology has important ramifications in the study of hydrogen-containing substances, including gas-storage and fuel-cell materials, systems with hydrogen bonds, and biological systems. Work published to date include model calculations on lithium hydride [1], hydrogen uptake by potassium intercalates [2], and hydrogen dynamics in the prototypical proton conductor caesium hydrogen sulphide [3]. Results of these studies have been presented at several seminars in the UK and abroad, as well as in Faraday Discussion 151 on Hydrogen Storage Materials (Rutherford Appleton Laboratory, April 2011) and the European Neutron Scattering Conference (Prague, July 2011). Brief summaries of the work accomplished to date are enclosed below.

3.6.1.1 *Model Calculations on Lithium Hydride and Deuteride: Comparison to NCS Experiments [1]*

Theoretical nuclear momentum distributions for solid lithium hydride and lithium deuteride were performed within the framework of plane-wave density functional theory, followed by the computation of phonon-dispersion relations and vibrational densities of states (see Figures 10 & 11 below). The computational results were compared with existing neutron Compton scattering and inelastic neutron scattering experiments on solid LiH. An excellent agreement between theory and experiment is found within the harmonic Born-Oppenheimer approximation. On the basis of the above, we estimate an upper conservative bound of 2 to 3% for the effects of non-adiabatic dynamics on the second moment and Laplacian of the atomic momentum distributions in this benchmark system. These results have important consequences and implications on future

theoretical studies of atomic momentum distributions from isolated molecules and extended condensed-matter systems.
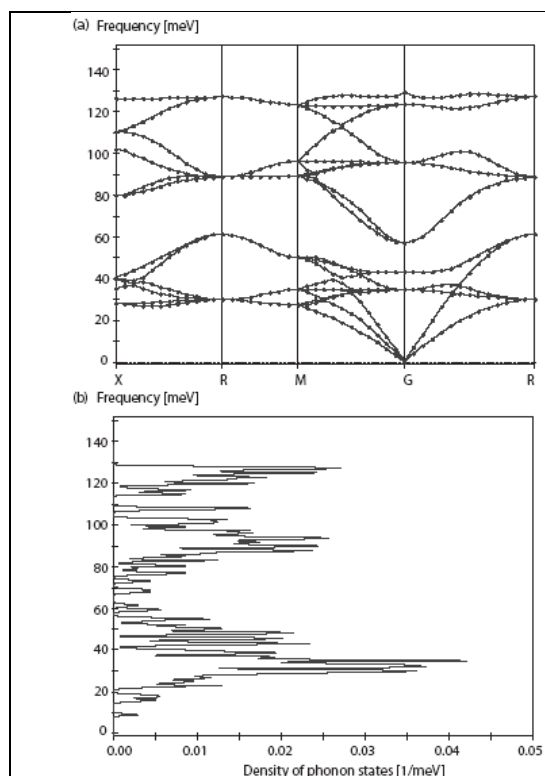

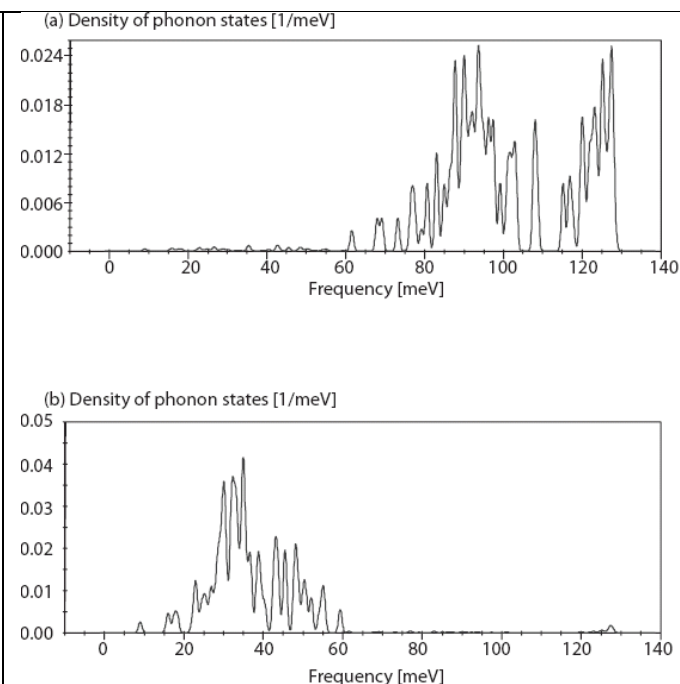**Figure 10: (a) LiH phonon dispersion and (b) total phonon density of states.**

Figure 11: Partial vibrational density of states in LiH. (a) H-projected and (b) Li-projected.

3.6.1.2 Uptake of Molecular Hydrogen by Alkali-graphite Intercalates [2]

The adsorption of molecular hydrogen (H_2) by the alkali-graphite intercalate KC_{24} was studied using neutron diffraction, NCS, and first-principles calculations using CASTEP on the SCARF cluster. Neutron Compton scattering data for the (H_2)xKC_{24} system (x=0-2.5) were measured at T=1.5 K as a function of the relative orientation between the neutron beam and the intercalate c-axis. Synchronous with the above proton recoil measurements, high-resolution diffraction patterns were measured in back-scattering geometry. The isotropic widths of the proton momentum distributions could be explained on the basis of three energy scales, namely, intramolecular H–H vibrations, followed by H–H librations and H_2 centre-of-mass translations (see Figure 12). From the coverage dependence of these neutron data, an upper bound of ca. 10 meV for intermolecular hydrogen-hydrogen interactions was also established. Finally, a weak anisotropy of the width of the proton momentum distributions was observed (see Figure 13). Comparison of these experimental data with first-principles predictions using CASTEP indicates that subtle quantum mechanical effects associated with particle delocalisation and exchange lie at the heart of the observed behaviour. These results provide an important stimulus for further work on ab initio nuclear momentum distributions, as the above mentioned quantum effects cannot be fully accounted for by assuming that hydrogen nuclei are classical particles.
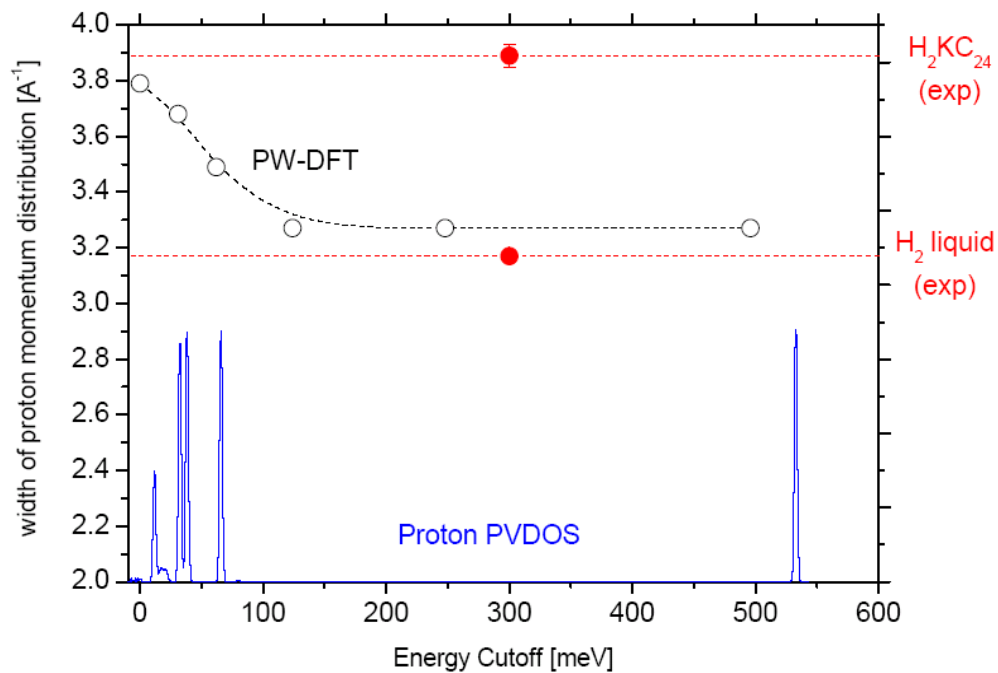
Figure 12: Dependence of the PW-DFT Compton profile on energy cutoff. The red traces indicate the experimental values for the isotropic Compton widths and associated uncertainties. The blue trace shows the partial vibrational density of states for hydrogen with an energy blurring of 1 meV.
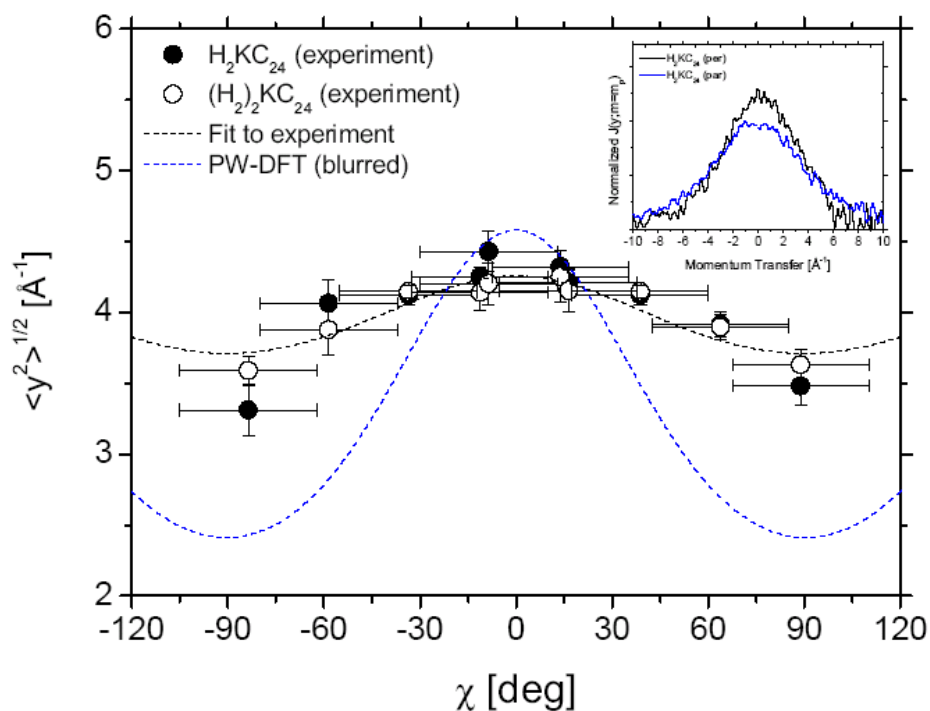

Figure 13: Dependence of proton Compton widths on orientation with respect to the intercalate c-axis for coverages x=1 and 2. The inset shows Compton profiles perpendicular (black) and parallel (blue) to the c-axis.

3.6.1.3 Hydrogen Dynamics in Solid Proton Conductors [3]

SCARF computational resources have been used to calculate momentum distributions in the solid proton conductor caesium hydrogen sulphide $CsHSO_4$. The motivation for this work has been threefold: (i) to assess the potential of NCS to explore hydrogen-migration mechanisms in solid proton conductors; (ii) to check the hypothesis that proton motions in $CsHSO_4$ are purely classical down to cryogenic temperatures, a task that can be accomplished by comparing measured and calculated proton momentum distributions to characterise the harmonicity of the effective Born-Oppenheimer potential; and (iii) benchmark first-principles computational models. PW-DFT electronic structure and phonon calculations using the CASTEP code within the GGA approximation have been performed for $CsHSO_4$ and compared with experimental NCS data. Linear-response phonon calculations were employed to obtain second moments of the nuclear momentum distribution (See Figure 14) using the methodology established and tested on lithium hydride [1]. Fair agreement with experimental values for the isotropic widths of the proton momentum distribution was achieved, yet the GGA appears to overbind the protons in their local effective potential. Our computational model was also used to dissect and understand experimental proton momentum distributions (See Figure 15). The relative contribution of different vibrations to the isotropic proton momentum distribution showed that NCS widths are dominated by modes in the region 130-250 meV. The picture that emerges from this work is quite different than that found for H2 adsorbed in KC24. In the latter case, NCS widths are dominated by the presence of a well-defined H—H stretch vibration around 500 meV, followed by much weaker modes all below 100 meV.
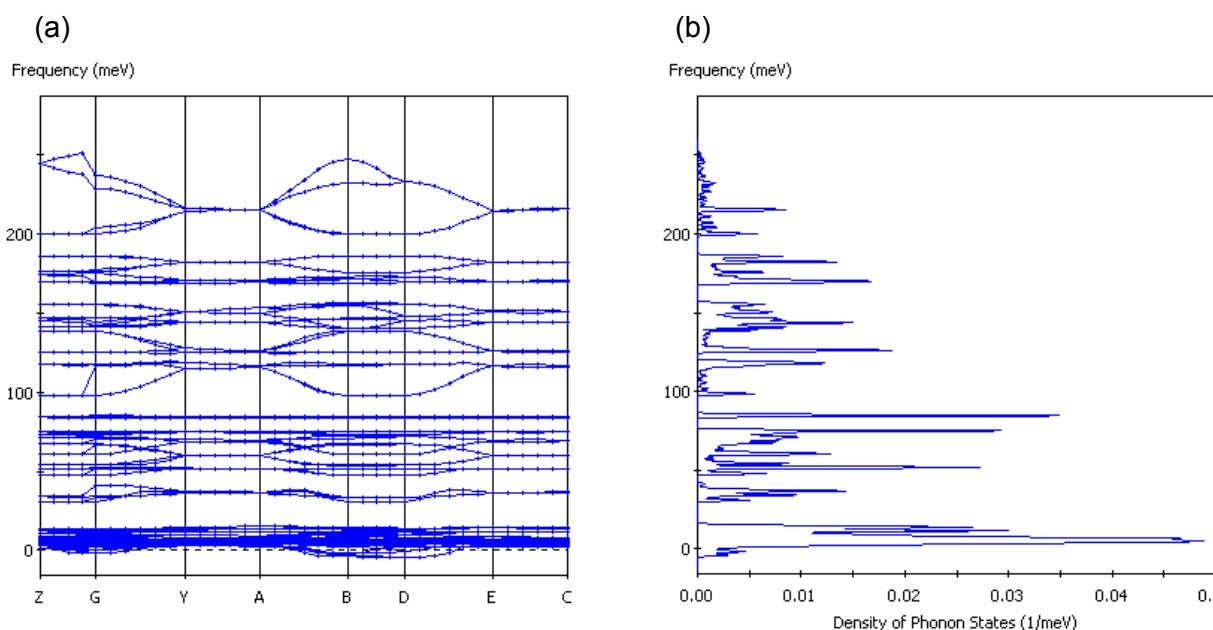

Figure 14: (a) caesium hydrogen sulphide CsHSO₄ phonon dispersion and (b) total phonon density of states calculated using the CASTEP code within the GGA approximation and the linear-response method.
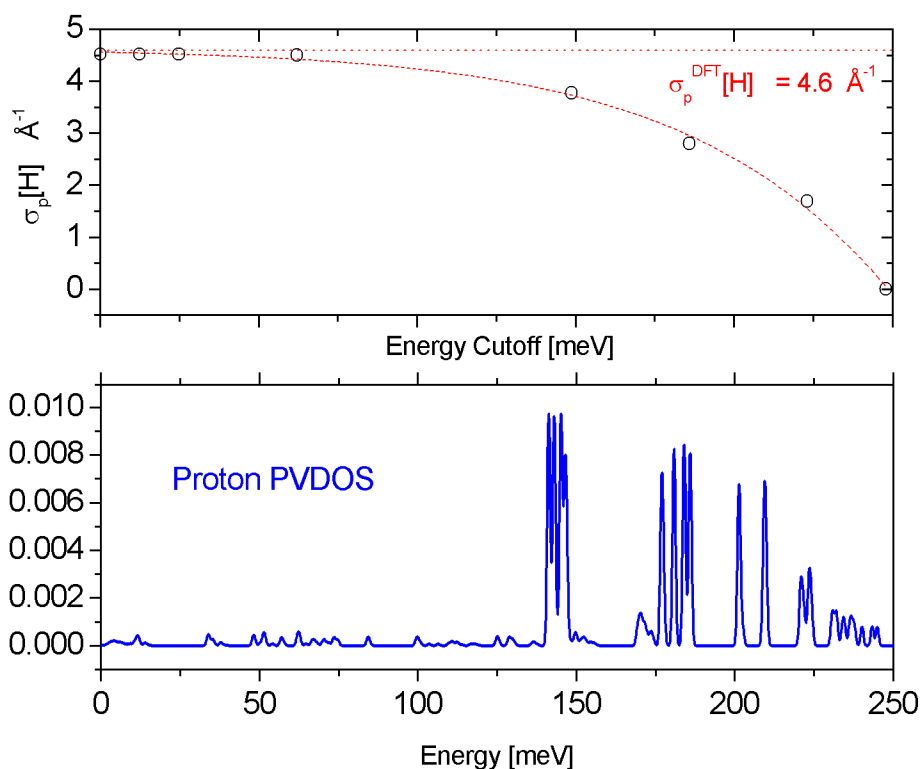
Figure 15: Dissection of calculated proton momentum distributions in CsHSO$_4$. The relative contribution of different vibrations to the isotropic proton momentum distribution shows that NCS widths are dominated by modes in the region 130-250 meV.

3.6.1.4 New Directions

Another use of the SCARF cluster relates to ab initio calculations of magnetic observables for the interpretation of NMR and neutron spectroscopic data. Here, the Gaussian 09 module has been used to calculate electric-field-gradient (EFG) tensor components to interpret NMR spectra and spin-lattice relaxation times in solid proton conductors. The motivation behind this study has been twofold: (i) to benchmark a new methodology that combines Gaussian 09 NMR GIAO calculations with the SPINACH program. SPINACH is a state-of-the-art Matlab library of functions for the very efficient (polynomial) ab initio prediction of NMR and ESR spectra on samples were neutron spectroscopic data are also available; and (ii) to perform a feasibility study of NMR-aided refinement of heavy-ion crystal structure in the solid super-proton conductor $(H_3O)SbTeO_6$. This second motivation is a particularly exciting one because Rietveld refinement of powder diffraction data can only provide mean statistical weights of Sb and Te occupancies. Ab initio calculations of NMR spectra, especially in the case of quadrupolar nuclei such as deuterons in D_3O+ ions, can in principle distinguish Sb and Te sites by comparing ab-initio deuterium quadrupolar coupling constants with values deduced from D-NMR spectra and spin-lattice relaxation time constants. Work is in progress to characterize deuterium NMR and QENS data on $(H_3O)SbTeO_6$ and $(D_3O)SbTeO_6$

1. M. Krzystyniak and F. Fernandez-Alonso, "Ab Initio Nuclear Momentum Distributions in Lithium Hydride: Assessing Nonadiabatic Effects," Physical Review B 2011 vol. 83 134305 (2011). [doi:10.1103/PhysRevB.83.134305]
2. M. Krzystyniak, M. A. Adams, A. Lovell, N. T. Skipper, S. M. Bennington, J. Mayers, and F. Fernandez-Alonso, "Probing the Binding and Spatial Arrangement of Molecular Hydrogen in Porous Hosts via Neutron Compton Scattering," Faraday Discussions 151 171-197 (2011). [doi: 10.1039/C1FD00036E].
3. M. Krzystyniak et al., in preparation.
4. "Molecular Hydrogen in Nanoporous Materials: Unveiling the Potential of Neutron Compton Scattering." M. Krzystyniak, M.A. Adams, A. Lovell, N.T. Skipper, S.M. Bennington, J. Mayers, and F. Fernandez-Alonso (presenter). Poster presented at the 5th European Conference on Neutron Scattering ECNS 2011, July 17-22nd 2011, Prague, Czech Republic.
5. "Proton Mobility in the Solid Super-proton Conductor CsHSO4." M. Krzystyniak (presenter), S. Richards, and F. Fernandez-Alonso. Poster presented at the 5th European Conference on Neutron Scattering ECNS 2011, July 17-22nd 2011, Prague, Czech Republic.
6. "Hydrogen Research with Neutrons: Why and How." F. Fernandez-Alonso. Invited seminar presented at the School of Physical Sciences, Nottingham Trent University, June 14th 2011, Nottingham, United Kingdom.
7. "Probing the Binding and Spatial Arrangement of Molecular Hydrogen in Porous Hosts via Neutron Compton Scattering." M. Krzystyniak, M.A. Adams, A. Lovell, N.T. Skipper, S.M. Bennington, and J. Mayers and F. Fernandez-Alonso (presenter). Talk presented at Faraday Discussion 151 – Hydrogen Storage Materials, April 18-20th 2011, Rutherford Appleton Laboratory, Didcot, United Kingdom.
8. "Hydrogen Research with Neutrons: From Protonics to Gas Storage." F. Fernandez-Alonso. Invited seminar presented at the Department of Chemistry Seminar Series, University of Sussex, Oct 27th 2010, Brighton, United Kingdom.
9. "How Quantum Mechanics Limits the Uptake of Molecular Hydrogen by Carbon-based Nanostructures." F. Fernandez-Alonso. Invited talk at the XV International Workshop on Quantum Atomic and Molecular Tunnelling in Solids and Other Condensed Phases, Sep 5-9th 2010, Darmstadt, Germany.

3.7 David S.D. Gunn, Ilian T. Todorov, John A. Purton (CSE)

3.7.1 *Defect Formation and Oxygen Vacancy Migration in $Gd_2Ti_2O_7$ and $Gd_2Zr_2O_7$ Pyrochlores*

The disposal and safe storage of nuclear waste is a significant challenge for the global community. Several of the radionuclides generated through the nuclear fuel cycle, such as ^{239}Pu and ^{235}U, have long half lives (24,100 years and 7×10^8 years respectively) and careful choice of suitable immobilisation matrices is crucial to prevent any environmental contamination. Such an immobilisation material must be able to withstand prolonged heavy ion particle bombardment while maintaining structural integrity. Pyrochlore-type compounds (see Figure 16) have been proposed as suitable host matrices for this purpose, and great attention has been paid to members of the series $Gd_2(Zr_xTi_{2-x})O_7(0 \quad x \quad 2)$. The radiation tolerance of this series increases with increasing zirconium content, and the healing process in the zirconate is expected to be faster than for the titanate as it does not undergo an amorphous transition upon radiation damage and is a fast ion conductor.
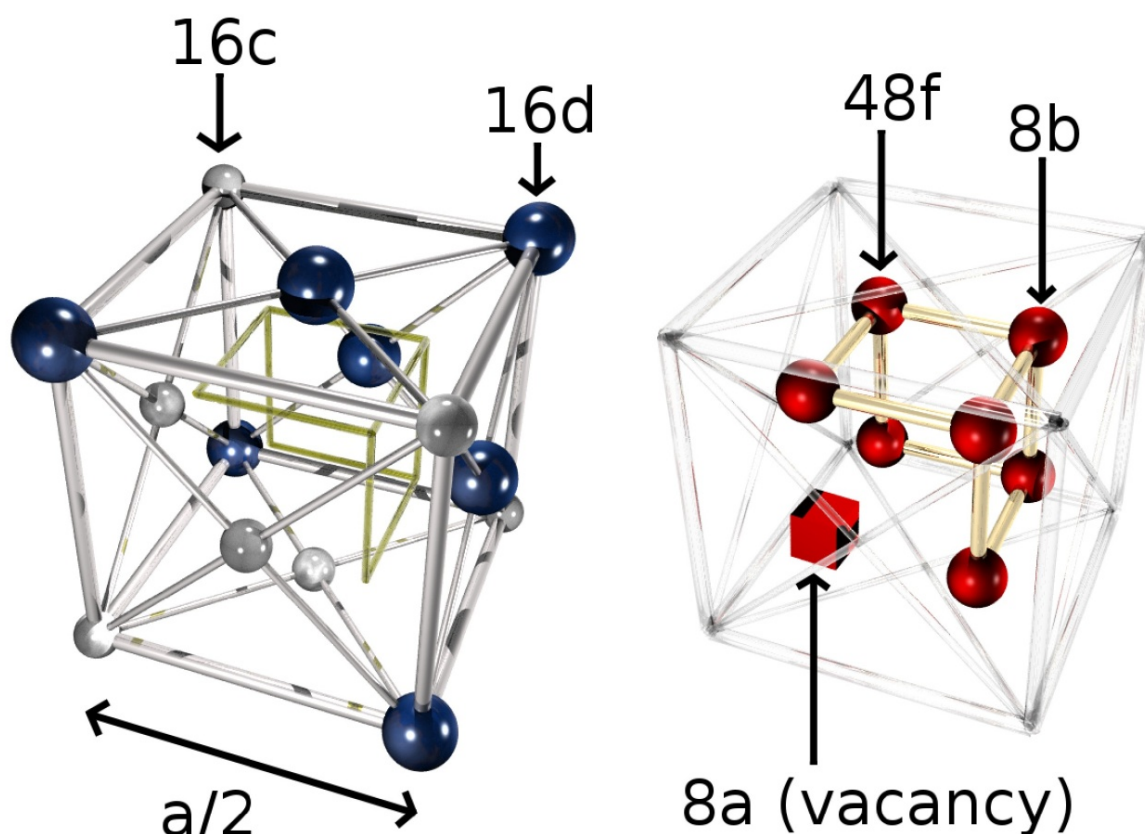
Figure 16: Schematic of one-eighth of the unit cell of a pyrochlore structure (Fd3m symmetry). The cation (left) and anion (right) sublattices are separated for clarity. Gd^{3+} ions are in blue, Ti/Zr^{4+} ions are in silver and O^{2-} are in red.

Our research has been focussed on developing a new set of Buckingham potentials, specifically tailored for looking at this $Gd_2(Zr_xTi_{2-x})O_7$ series. In particular, careful attention is paid to defect formation energies and oxygen vacancy migration activation energies so that a clear fundamental understanding of the process of damage formation and healing is obtained. The simplest oxygen vacancy migration mechanism in pyrochlores consists of sequential movements of oxygen ions from an occupied 48f position to a vacant 48f position. This usually occurs either through a straightforward activated hopping process, or via a slightly more complicated split-vacancy intermediate (see Figure 17).

The calculated titanate activation energy of 0.29 eV for the oxygen vacancy migration is in keeping with the values calculated using similar methods with other potentials, but remains substantially lower than a value obtained by extrapolation of experimental conductivity values for the series $Gd_2(Zr_xTi_{1-x})_2O_7$ (x=0.25-1.00). We are now performing equivalent *ab initio* calculations using the ABINIT code to provide further comparison for our atomistic work. Initial results from these simulations are promising, and have successfully calculated physical properties and cation antisite defect energies consistent with experimental values and those in the literature.
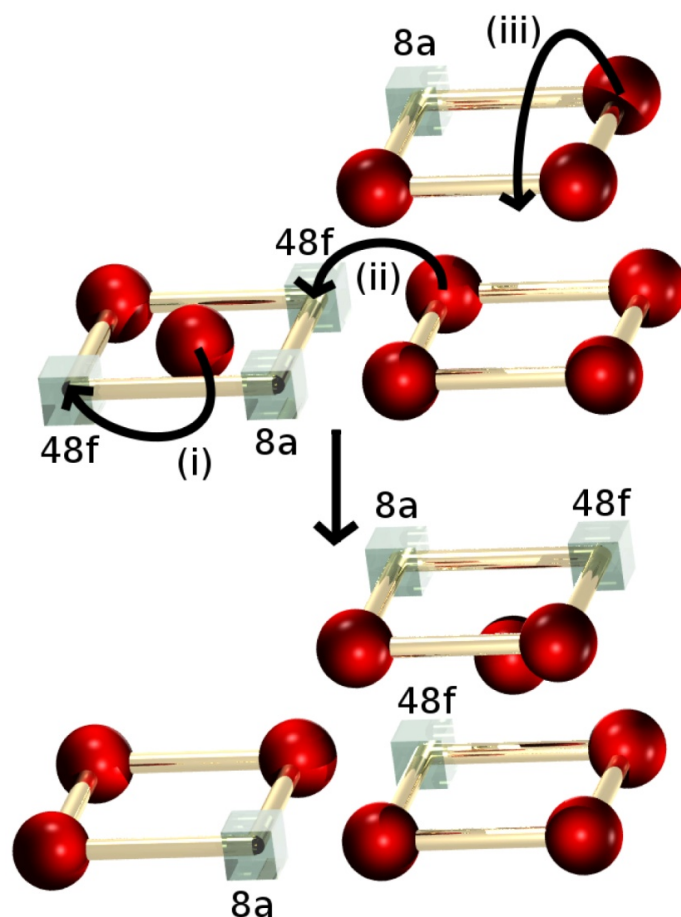
Figure 17: The mechanism of the split-vacancy oxygen migration. Red spheres represent O^{2-} ions, and the transparent cubes are oxygen vacancies. In (i) the interstitial oxygen moves to a vacant 48f position. In (ii) an oxygen in a 48f position hops into the remaining 48f vacancy from the split vacancy. In (iii) A new split vacancy is formed with an oxygen moving from 48f into an interstitial position.

3.8 Stewart Parker (ISIS)

3.8.1 Inelastic neutron scattering spectroscopy (INS)

The ISIS Facility at RAL is the world-leading centre for neutron vibrational (INS) spectroscopy of materials. One of the advantages of INS is that it is straightforward to compare the results of ab intio calculations with the experimental data. This is a synergistic process: comparison of observed and calculated spectra is a exacting test of the calculation, while the calculation provides unambiguous assignments of the spectra. We have used SCARF to analyse two systems that have been controversial: lithium hydroxide monohydrate, LiOH.H$_2$O and the iconic molecule buckminsterfullerene. C$_{60}$. For both systems we have used periodic density functional theory using the CASTEP code on SCARF. For LiOH.H$_2$O we were able to show that all previous work based on empirical criteria was, at least partially, incorrect. The librational modes of water do not follow the expected rock > wag > twist order and the calculations showed that the usual methods of assignment based on complete or partial deuterium substitution would not be useful. In order to model the spectra successfully, it was essential to include the strong dispersion present in the modes. This is shown in the left side of Fig. 1 where a comparison of the observed (middle) and scaled (by 0.95) CASTEP calculated INS spectra of ^{7}LiOH·H$_2$O: (lower) Γ-point only and (upper)

including dispersion across the Brillouin zone is shown. The right side of Fig. 18 shows the dispersion curves of ^{7}LiOH·H$_2$O in the 0–1200 cm^{-1} region as calculated by CASTEP.
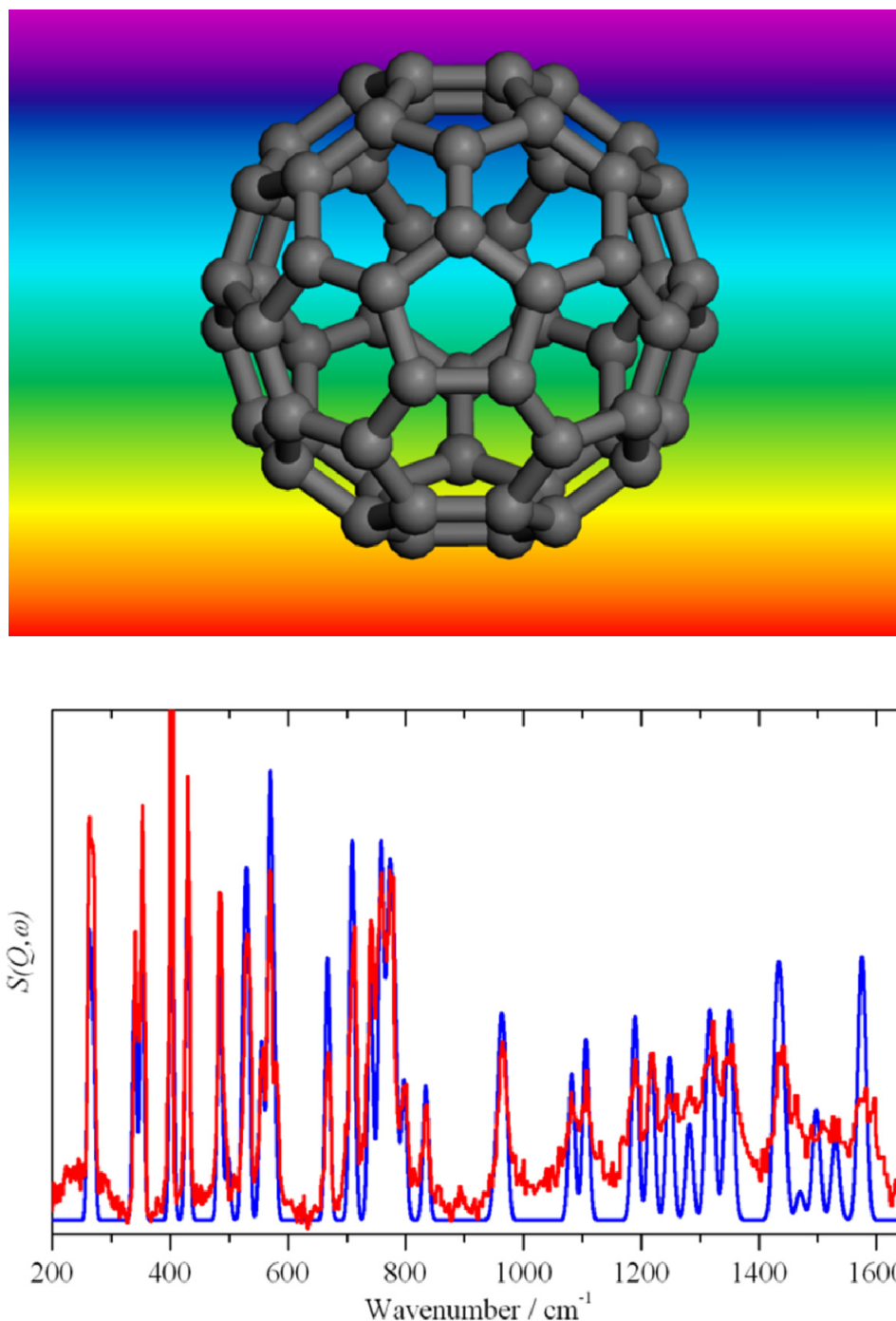

Figure 18: Top: Comparison of the observed (middle) and scaled (by 0.95) CASTEP calculated INS spectra of ^{7}LiOH·H$_2$O: (lower) Γ-point only and (upper) including dispersion across the Brillouin zone. The calculated spectra include overtones and combinations up to n = 10. Bottom: Dispersion curves of ^{7}LiOH·H$_2$O in the 0–1200 cm^{-1} region as calculated by CASTEP

The icosohedral molecule C$_{60}$ is one of the defining structures in chemistry and the assignment of the vibrational spectrum has been debated ever since it first became available in macroscopic quantities. The 174 internal degrees of freedom are grouped into 46 modes of which only 14 are

formally allowed in the infrared or Raman spectrum. It was realised early on that all the modes are allowed in INS spectroscopy and INS spectra from small quantities, ~1 g or less, were obtained by several groups at low to medium resolution, most are characterised by, at best, modest signal-to-noise ratio. We have repeated the INS measurements but with a large, 13 g, sample and under conditions of the highest available resolution and signal-to-noise ratio. SCARF has enabled us to use CASTEP to analyse both solid state phases of C_{60}, one of these contains four molecules in the unit cell and is the first time it has been modelled. Our assignment differs from all previous work, however, it is the only one that is able to successfully reproduce the INS spectrum in terms of both transition energies and intensities, as shown in Figure 19.
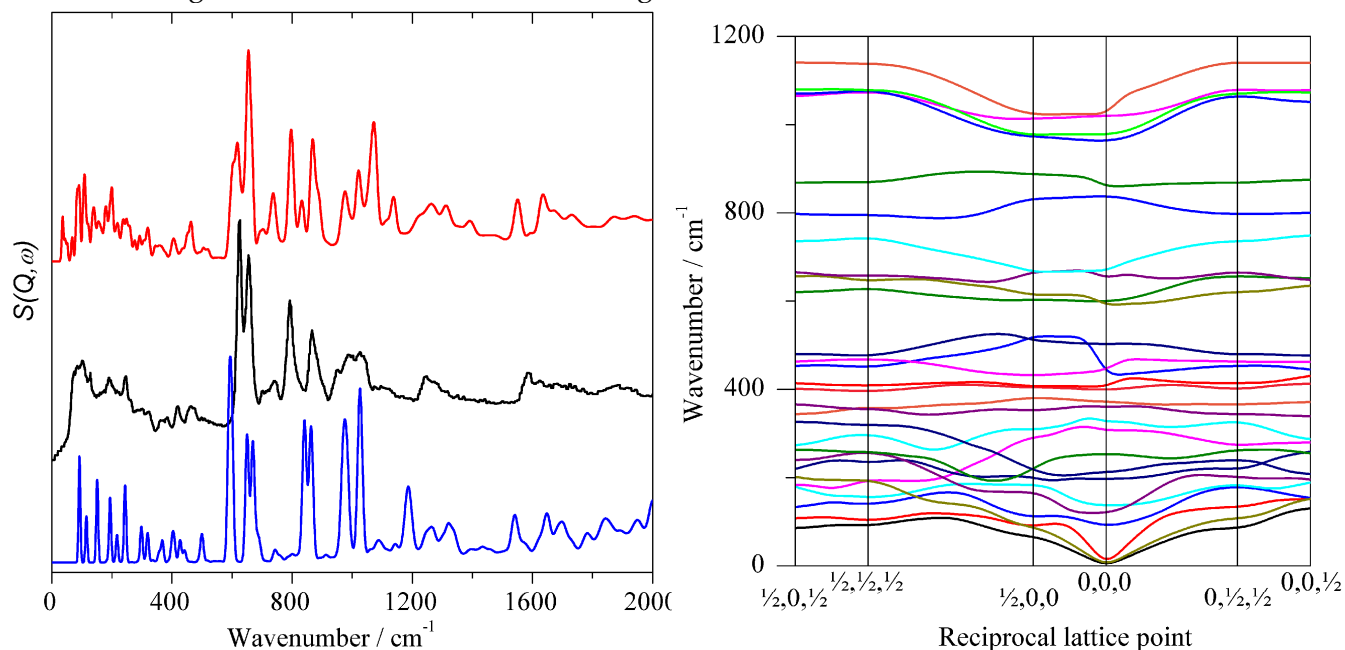

Figure 19: INS spectrum of the internal modes of C_{60} in the $Pa\overline{3}$ phase: recorded on TOSCA at 20 K (red) compared with the spectrum generated from a scaled CASTEP performed on SCARF (blue).

3.9   R.H.H. Scott,[1, 2, a)] C.P. Ridgers,[3, 2] R.M.G.M. Trines,[1] M. Tzoufras,[3, 1] S.J. Rose,[2] and P.A. Norreys[1, 2]

[1)]*Central Laser Facility, STFC, Rutherford Appleton Laboratory, Harwell Oxford, Didcot, OX11 0QX, United Kingdom*
[2)]*Department of Physics, The Blackett Laboratory, Imperial College London, Prince Consort Road, London, SW7 2AZ, United Kingdom*
[3)]*Clarendon Laboratory, University of Oxford, Parks Road, Oxford OX1 3PU, United Kingdom*

3.9.1   *Modelling the Effect of Density Scalelength on the Fast Electron Beam Generated by Ultra-Intense Laser-Solid Interactions*

This work was performed as part of a systematic investigation into the understanding of ultra-intense laser- solid interactions with particular focus on fast ignition relevant conditions. 2D3P particle-in-cell modelling using the osiris code showed that when density gradient on the target front surface (the density scale length) is sufficiently large, the fast electron beam resulting from the laser-solid interaction is best described by two distinct populations: those accelerated within the

sub-solid density plasma - the fast electron pre-beam, and those accelerated near or at the target front surface - the fast electron main-beam. The pre-beam has considerably lower divergence than that of the main-beam with a half-angle of ~ 20° under the conditions investigated it contains up to 30% of the total fast electron energy absorbed into the target. The fast electrons comprising the pre-beam have a higher temperature than those of the main-beam. The number, kinetic energy, and total energy of the fast electrons in the pre-beam is increased by an increase in density scalelength.

A larger density scalelength reduces the total number of electrons absorbed into the target, but increases their mean kinetic energy, while the total absorbed energy is unchanged. With a larger density scalelength, the fast electrons heat a smaller cross sectional area of the target, causing the thinnest targets to reach significantly higher rear surface temperatures. This is ascribed to the enhanced fast electron pre-beam associated with the large density scalelength interaction, which generates a magnetic field within the target of sufficient magnitude to partially collimate the subsequent, more divergent, fast electron main-beam.

A grid of 26800 x 10000 cells (16 electrons and 1 ion per cell) were used over a real space of 270 x 100 µm. This resolved the plasma wavelength 19 times at the peak density of 40 times critical (n_c). The time-step satisfied the 2D Courant condition, resolving the peak plasma frequency 27 times per time-step. Each run lasted a real time of 1.5 ps and took 1150 cpu-days.
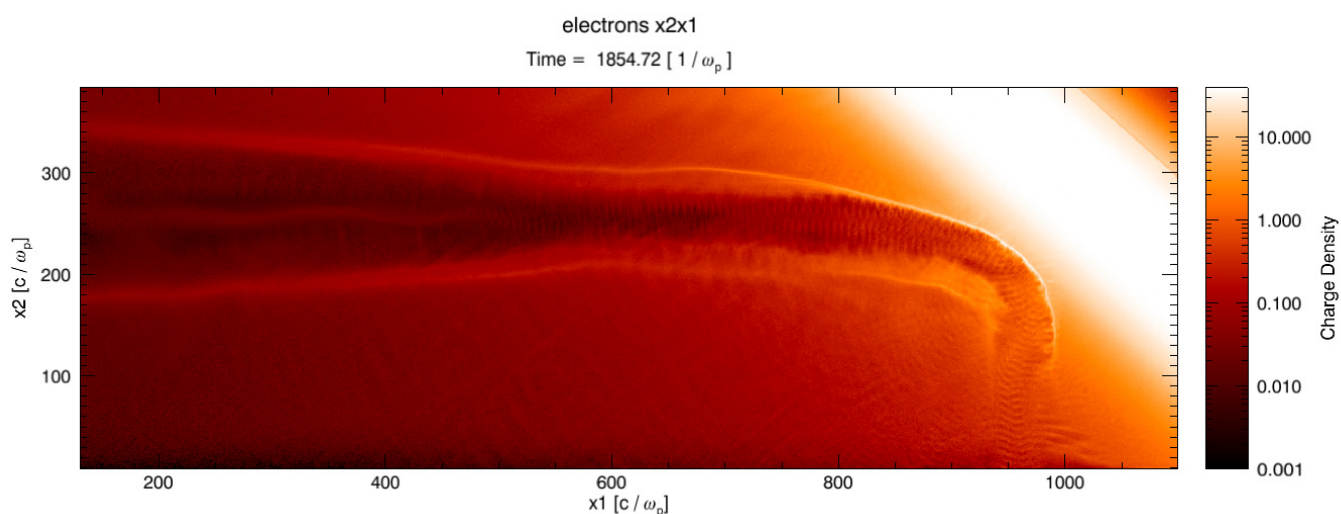

Figure 20: Channelling by, and subsequent refraction of the laser light within the large density scalelength underdense plasma as it approaches the 45° p-polarised 40n_c target (top right). Only part of the simulation box is shown.
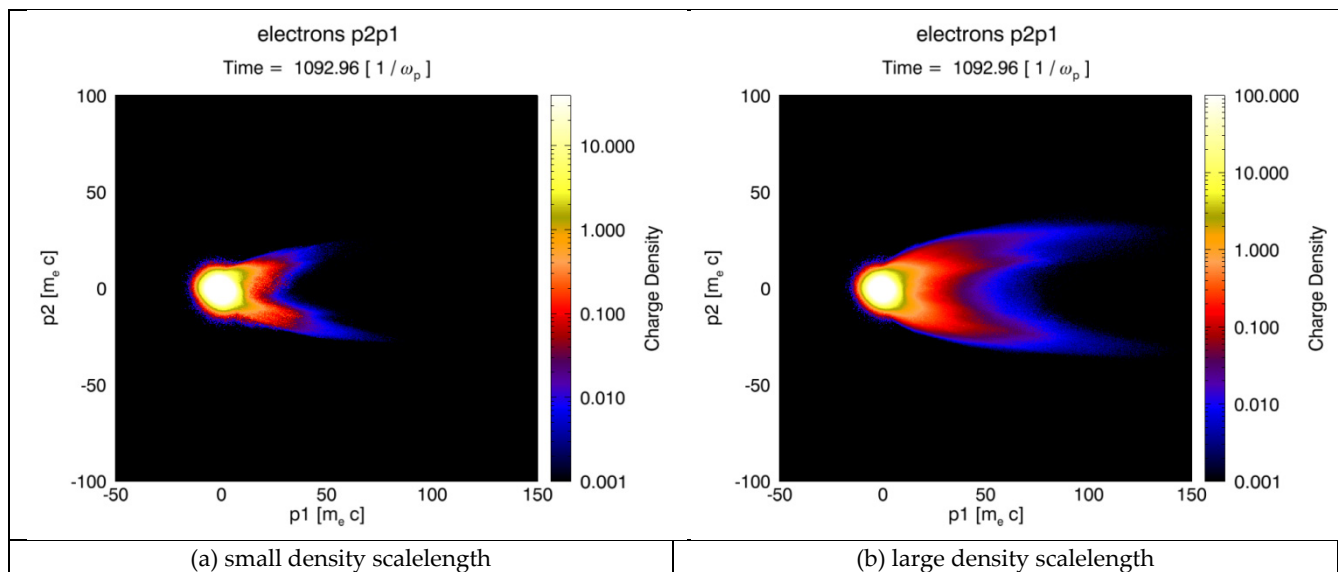
| (a) small density scalelength | (b) large density scalelength |

Figure 21: Phase space plots showing the momentum components parallel (p1), and transverse (p2), with respect to the laser injection axis at time $1035\omega_p^{-1}$ - the pulse is at $0:5n_c$, just 4 µm from n_c

3.10   Rowan Hargreaves (ISIS)

3.10.1 *The atomistic structure of a micelle in solution determined by wide Q-range neutron diffraction*

There is significant interest in the application of self-assembled structures in nanotechnology as they provide a means for the material scientist to build from the bottom up. Specifically, they have found use either as a means to encapsulate other chemical species (for example, they can act as a vector for drug molecules, increasing their solubility and stability) or as soft-templates to direct the fabrication of nano-structured materials (for the use in solar cells, batteries, molecular sieves and catalysts). Surfactant micelles are the prototypical example of a self-assembled structure -- the surfactant molecules self-assemble into a spherical aggregate in solution driven by the conflicting affinity of their head and tail groups with the solvent. The exact size and shape of the micelle is determined by a number of factors, including the type of surfactant, its concentration, the temperature, the pH and the action of salt and other co-solutes.

Wide Q-range neutron diffraction measurement on disordered materials, like liquids and glasses, provides structural information on length scales from the atomic to the mesoscopic. By making isotopic substitutions to the sample we are able to alter the contribution from the different components in the sample to the measured diffraction signal. So, in making measurement on a series of isotopically-substituted samples--that are otherwise chemically equivalent--we gain considerable detail of the structure of the sample. The real power of this technique is that the

measured data can be interpreted using the molecular modelling technique Empirical Potential Structure Refinement (EPSR). EPSR is a Monte Carlo simulation driven by the diffraction data and constrained by known physical properties of the system, like the density, composition and stochiometry. It produces 3D configurations of the molecules in the system that are as consistent as can be with the experimental measurement.

We have already used SCARF to run EPSR models of small surfactant micelles [1]. Starting from an initially disordered configuration, driven by the diffraction data, EPSR was able to assemble a micelle of size, shape and composition consistent with other experimental studies. It was found that the surfactant tail groups are hidden away from the solvent to form a central "dry" hydrophobic core, which is surrounded by a disordered corona containing the surfactant headgroups, counterions, water and some of the alkyl groups from the hydrophobic tails. This combination of wide Q-range neutron diffraction and molecular modelling provided us with a complete description of the structure of the micelle in solution; it gives us both the large scale features of the micelle and the atomistic detail of the molecular interactions that are responsible for the self-assembly.

Having access to SCARF allowed us to run many EPSR simulations in parallel to test different models and data correction methods, and to address finite size effects and issues of sampling in these slowing equilibrating systems. We are currently continuing our study of the surfactant micelle systems by looking at the effects of increasing temperature, changing the concentration of surfactant, and adding different counterions. (Figure 22 shows some snapshots of the micelles we have observed in our preliminary simulations.)

This work on the surfactant micelles has proved the value and viability of this technique. We are now looking to apply it to other disordered systems, where an understanding of both their large scale structure and the details of the chemical interactions are required.
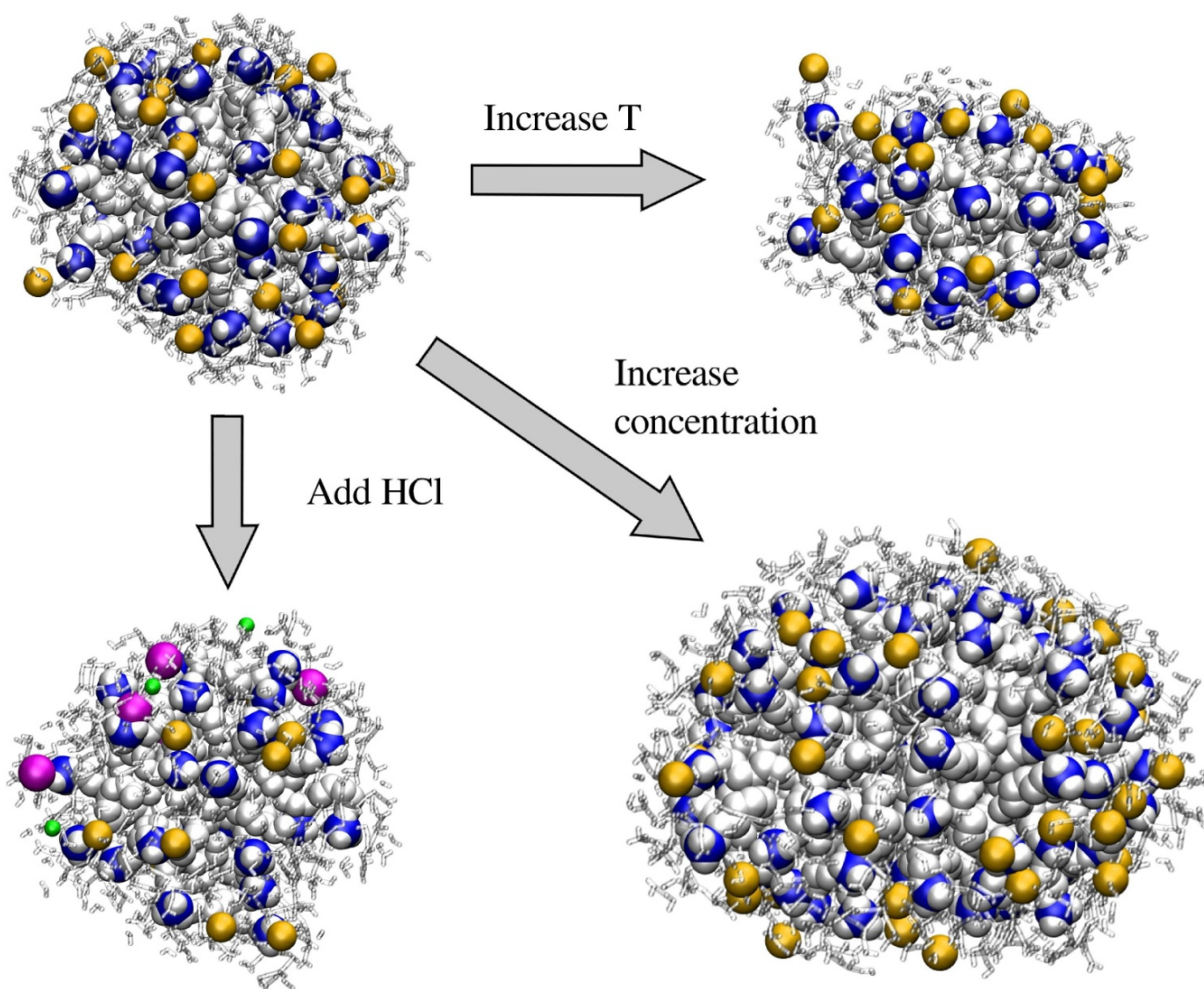
Figure 22: Snapshots from EPSR simulations of C10TAB micelles showing the effect of increased temperature, concentration and adding HCl on the micelle.

1. *The atomistic structure of a micelle in solution determined by wide Q-range neutron diffraction* Rowan Hargreaves, Daniel T Bowron and Karen Edler, **JACS** ,2011, Just accepted, **DOI:**10.1021/ja205804k

3.11   Andrea Ferretti[1-2], Giuseppe Mallia[3], Layla Martin-Samos[4], Giovanni Bussi[5] Alice Ruini[2-1], Barbara Montanari[6] and Nicholas M. Harrison[7-3]

[1]*Centro S3, CNRâ€"Istituto Nanoscienze, I-41125 Modena, Italy.*
[2]*Dipartimento di Fisica, Universit` di Modena e Reggio Emilia, I-41125 Modena, Italy.*
[3]*Department of Chemistry, Imperial College London, London SW7 2AZ, UK.*
[4]*DEMOCRITOS National Simulation Center, CNR IOM Istituto Oﬁcina dei Materiali, I-34014 Trieste, Italy.*
[5]*SISSA, I-34014 Trieste, Italy.*
[6]*Computational Science and Engineering Department, STFC Rutherford Appleton Laboratory, Oxfordshire OX11 0QX, UK.*
[7]*Computational Science and Engineering Department, STFC Daresbury Laboratory, Cheshire WA4 4AD, UK.*

3.11.1 *Electronic transport: ab initio complex band structure of conjugated polymers. Effects of hybrid DFT and GW schemes.*

The fields of molecular electronics and charge transport through nano-junctions has been deeply investigated in the past fifteen years. At the experimental level many different techniques have been developed, including those based on break junctions, nanostructured and scanning probe layouts, or self-assembled monolayers. Measurements have been performed on a number of systems ranging from saturated olephins (alkanes) to biological molecules} (such as DNA). Theoretically, the mechanism underlying these experiments can be understood by separating the effect of the electronic structure of the insulating layer (i) through the calculation of the complex band structure (CBS), or evanescent states, in the limit of an infinitely long insulating region. The CBS approach is also particularly interesting for an ab initio evaluation of beta, where the calculations can be performed either using wave function or green's function-base approaches. A cartoon describing the relation between the electronic structure of the MIM junction and the evaluation of the beta-decay factor is given in Figure 23.
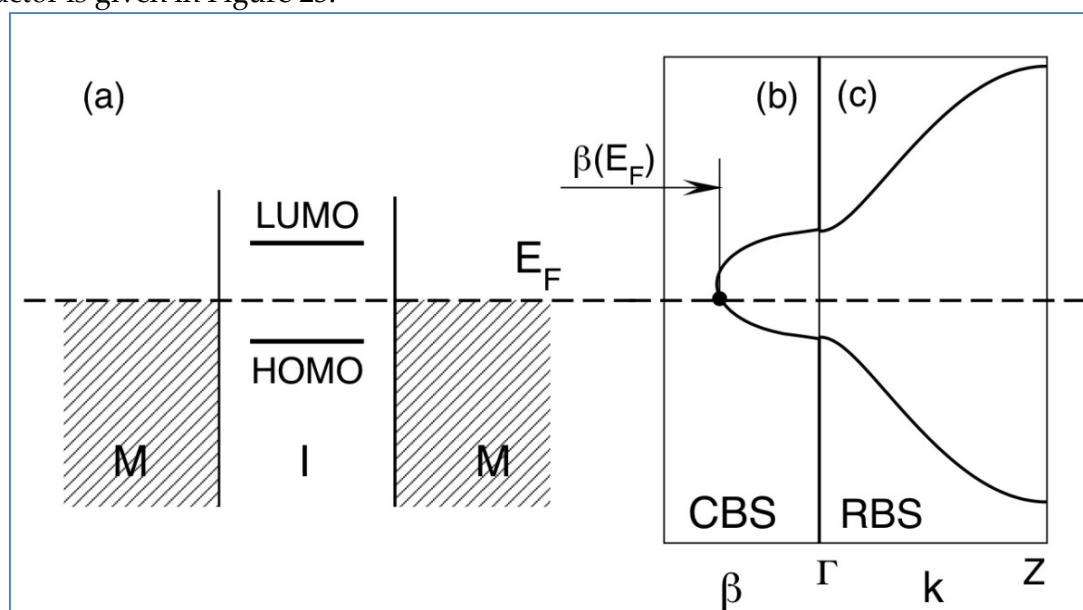

Figure 23: The non-resonant tunnelling experiment. (a) Scheme of the alignment of electronic levels in a metal-insulator-metal (MIM) junction. The complex and real band structure (CBS and RBS) corresponding to the (extended) insulator system are reported in (b) and (c) respectively. The computed value to be compared with experiments is highlighted as beta(E_F), E_F being the Fermi energy of the MIM junction.

We have numerically investigated four polymers, namely poly-ethylene (PE), poly-acetylene (PA), poly-para-phenylene-vinylene (PPV), and poly-phenylene-imide (PPI). In this work, DFT and hybrid-DFT calculations have been performed using the CRYSTAL09 package. The code implements all-electron electronic structure methods within periodic boundary conditions and adopts an atomic basis set expanded in Gaussian functions. Once the Hamiltonian matrix elements are obtained, the real and complex band structures are interpolated using the WanT package. Differently, GW results have been obtained using the plane-waves and pseudopotentials implementation of SaX, which is interfaced to Quantum-ESPRESSO for what concerns DFT calculations. In this case, once the Kohn-Sham electronic structure is evaluated, we first compute maximally-localized Wannier functions using WanT and then apply the CBS technique.

Our results for four polymers (namely poly-ethylene, poly-acetylene, poly-para-phenylene-vinylene, and poly-phenylene-imide) compare well with the existing theoretical and experimental literature. In particular we find that PBE0 results are those most resembling the G0W0 electronic structure. This suggests PBE0 as a cheaper alternative to GW for these class systems. The same is true both for the real electronic structure and for the comparison with transport data (when available), where the limitations of LDA/GGA functionals in describing transport at the Landauer (non-interacting) level are well known.

3.12   Andrew Seel (ISIS, Oxford)

3.12.1   *Calculation of phonon states and modelling of inelastic neutron spectra (INS)*

Our work utilizes SCARF for the calculation of phonon states and modelling of inelastic neutron spectra (INS) for various porous materials containing a low concentration of hydrogen containing molecules. Recently we have been examining the coordination of ammonia within small-pore zeolite hosts, NaA and CuA. Fully periodic density functional calculations are carried out using the CASTEP code in order to suggest structure, and optimize the systems with no restraint of symmetry. Often there is appreciable disorder in the systems at low concentrations of absorbed small-molecules that crystallographic data is not available. Phonon calculations are then performed and the hydrogen-weighted density of states extracted, with INS modelling subsequently being carried out using the aClimax code.

We are particularly interested in how coordination of the small molecule to extra-framework cations affects the INS spectra through non-isotropic molecular recoil, coupling to framework phonons, and the effect of hydrogen-bonding on the librational dynamics. Currently we are extending this research to incorporate quasi-elastic neutron data to compare with calculated activation energies for longer-timescale processes of the coordinated ammonia.
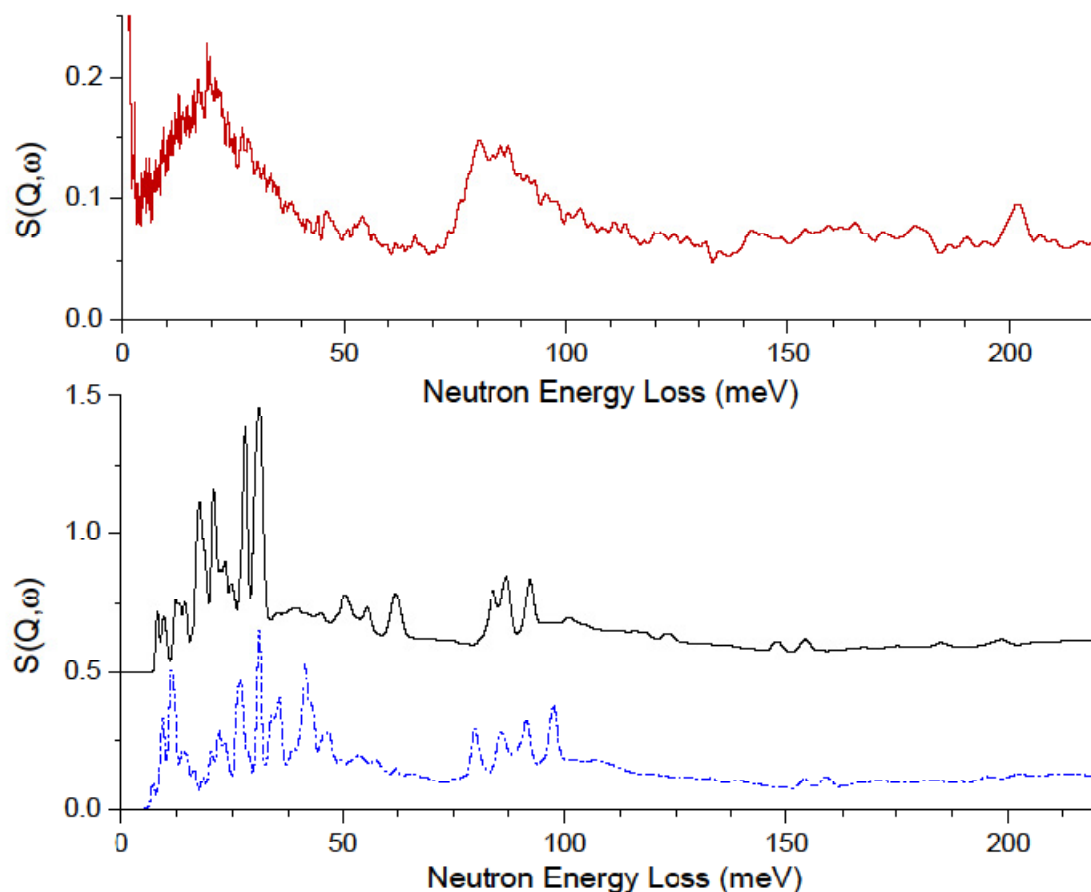
Figure 24: Top: measured INS spectrum of ammonia absorbed at low concentrations within zeolite CuA. Bottom: modelled INS spectra for ammonia coordinated to extra-framework copper cations in a single, tetragonal arrangement (black) and a double, planar arrangement (blue)

3.13 Toyoto Sato,*† A.J. Ramirez-Cuesta (ISIS) ‡ Kazutaka Ikeda,§ Shin-ichi Orimo and Kazuyoshi Yamada†,

3.13.1 Ab-Initio calculations of the dynamics of select Hydrogen containing materials, compared to Inelastic Neutron Scattering Spectra.

The nature of the interaction of neutrons with matter, make neutrons an ideal tool for studying the structural and dynamical properties of materials. Because of their wavelength, thermal neutrons can also simultaneously measure structure and dynamics. In inelastic spectroscopy the scattering process conveys information on the dynamics across the Brillouin zone and it has no selection rules, unlike Raman and Infrared spectroscopy (IR) making the assignment of the spectra relatively straightforward. The incoherent cross section of hydrogen is over 20 times larger than most chemical elements. This makes incoherent inelastic neutron spectroscopy (INS) a very powerful tool to observe the dynamics of hydrogen containing materials. We have used ab-initio density functional theory (DFT) calculations to study the dynamics of a host of hydrogen storing materials, from light metal hydrides to metal-organic frameworks (MOF's).
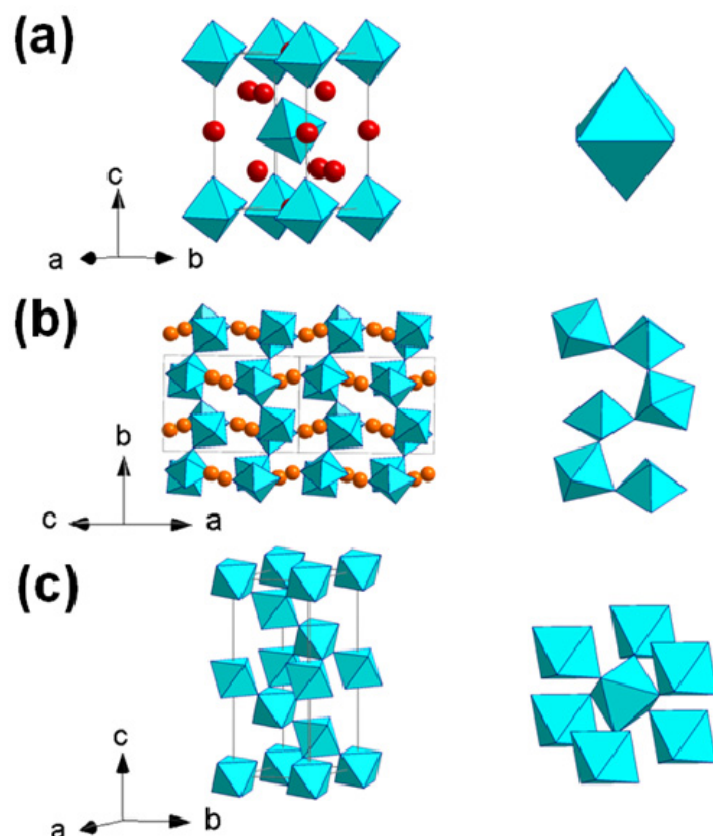
Figure 25: Crystal structures of (a) Na$_3$AlH$_6$ (b) CaAlH$_5$ and (c) α-AlH$_3$

We performed a combined study using inelastic neutron scattering (INS) and first-principles calculations of the vibrational properties of CaAlH$_5$, Na$_3$AlH$_6$ and α-AlH$_3$ with different AlH$_6$ networks, a zigzag one-dimensional AlH$_6$ network for CaAlH$_5$ and a three-dimensional AlH$_6$. (Structure shown in Figure 25) Combining the INS and the DFT results with CASTEP we determine the correlation between frequency and bond length shown in figure 27. The quality of the calculation can be easily seen in figure 26 where the INS is compared with the calculation of the spectra and of the phonon dispersion curves.
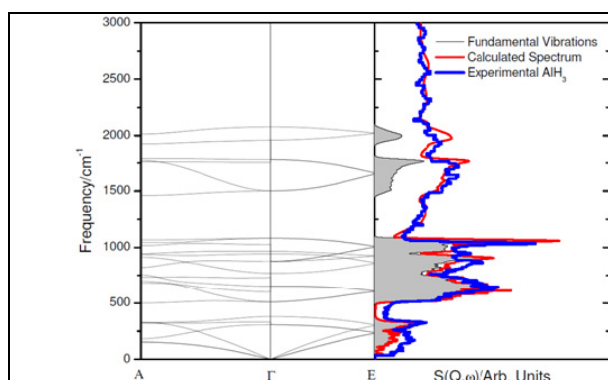
Figure 26: The experimental (blue line) and total calculated (red line) INS spectra of α-AlH3 (right side) with the calculated phonon dispersions (left side).
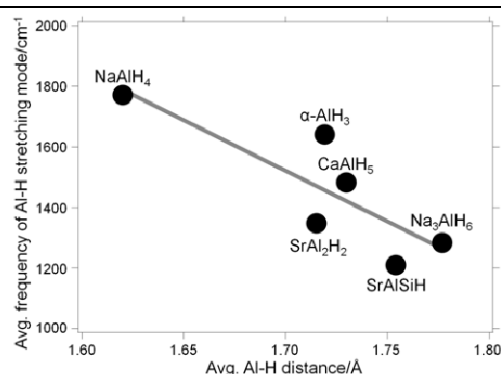
Figure 27: Correlation between the averaged frequencies ω_S (Al-H bond-stretching modes) and averaged Al-H bond distances.

3.14   C W Yong (CSE)

3.14.1   Molecular dynamics simulations of MgO cluster impact on Al (111) surface

Molecular dynamics (MD) simulations have been carried out to study the bombardment of ionic $(MgO)_{28}$ nano-cluster projectile upon Al(111) surface, simulating the micro-meteorite impact on metal surfaces. Two different impact energies have been considered, 50 eV and 1 keV. Both cases show very different impact behavior where the MgO projectile remains largely intact for the lower energy case, whereas the MgO projectile fragments upon higher energy impact. Partial surface healing is taken place as the energy is dissipated and formed a permanent crater near to the surface. The healing process is impeded due to the implantation of MgO fragments within the surface bulk near to the impact crater. These findings have significant implication in assessing the structural performance of materials that are exposed to extreme environment such as outer space.
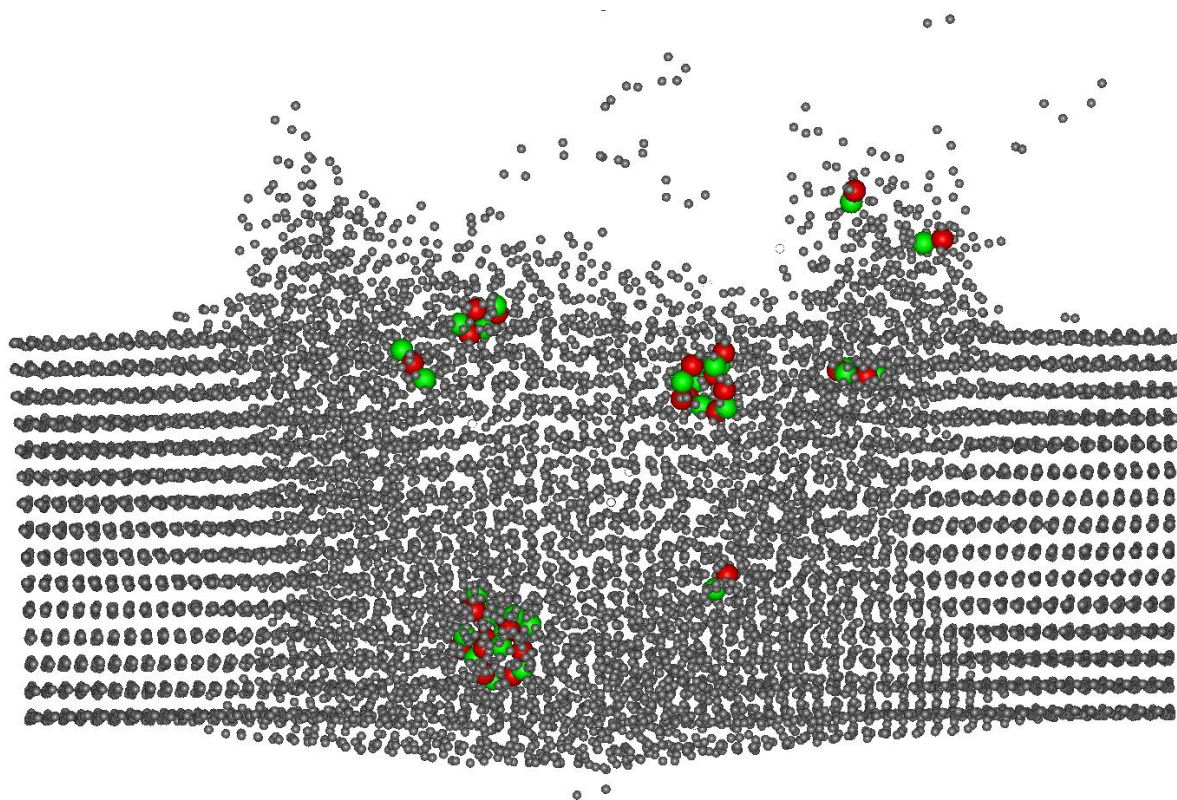
Figure 28: The picture shows a still instantaneous bombardment process of 1 keV MgO nanocluster at 0.3 ps after impact on Al(111) surface, creating a micro-explosion at the surface and fragmented the cluster. The model consists of 457000 atoms running using DL_POLY_4. The picture only shows part of the surface model where actual bombardment was taken place.

3.15 Enrique Sanchez Marcos (Univ.Sevilla), Elisa I. Martin (Univ.Sevilla), Keith Refson (STFC. CSE)

3.15.1 *Ab initio Molecular Dynamics Simulations of N-coordinated Cu(II) complexes in water*

Copper is one of the most abundant transition metal ions present in the human body. Its coordination to different biomolecules is responsible of many important physiological processes. Abnormal interactions seem to be at the heart of several neurodegeneratives diseases. One of the most frequent Cu(II) coordination mode involves nitrogen-containing ligands, adopting an average square-planar arrangement. This study has undertaken the theoretical description of one of its representative complex in water, bis-ethylenediamine-Cu(II) $[Cu(C_2N_2H_8)2]^{2+}$, (Figure 29) by using Born-Oppenheimer Molecular Dynamics. This provides information about two keys issues in the understanding of the chemical behaviour of this metal cation in biochemical media:a)the hydration structure, namely the solvation pattern of the water molecules in the axial and equatorial regions surrounded the planar complex; b) the solvent effects on physicochemical and spectroscopical properties of the complexes.

CASTEP, the UK's premier plane-wave DFT modelling code, provides a suitable tool to fulfil these objectives. This study represents one of the first tests of CASTEP applications on liquid solutions. BOMD simulations (NVT) of one Cu(II) complex and 80 H_2O, using the PBE functional have been carried out. The importance of dispersion contributions to the system has been analyzed by means of a parallel BOMD simulation, where a recent corrected-PBE method including van der Waals interactions was incorporated. Total simulation times were 35ps.

Structural results show an asymmetric axial hydration, where one water molecule coordinates Cu(II) (~2.5 Å) on one side of the molecular plane of the metal complex, while on the other side of the plane, the water molecules are much weakly coordinated (~ 3.5 Å). (Figure 29). This asymmetric axial hydration is more pronounced when the dispersion term is included in ab initio simulations.
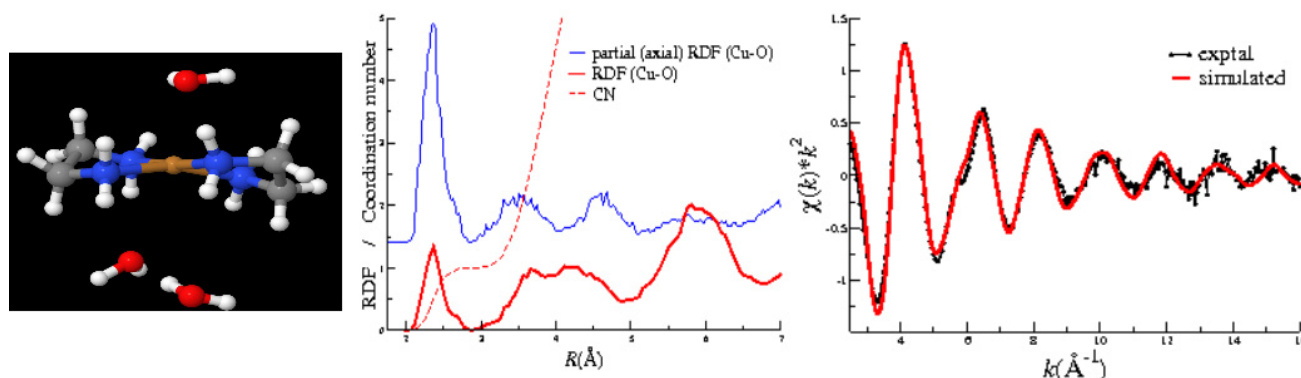
Figure 29: bis-ethylenediamine-Cu(II) $[Cu(C_2N_2H_8)2]^{2}$ using Born-Oppenheimer Molecular Dynamics

From a set of evenly spaced snapshots, an average simulated EXAFS spectrum of the Cu K-edge has been computed by using the FEFF (version 9.0) code. The good agreement with the experimental spectrum supports the good microscopic description provided by BOMD simulations for this type of systems.

3.16   Bin Qiao(QUB), Macro Borghesi (QUB), Matthew Zepf (QUB), David Neely (STFC)

3.16.1   *Scarf Usage summary of Queens University Belfast plasma physics*

In the past year we have done particle-in-cell (PIC) modelling in a number of areas of intense laser matter interactions on the SCARF cluster at Rutherford Appleton Laboratory. This includes laser-driven ion acceleration, high-harmonic generation, and generation of relativistic electron mirrors. All these simulations have helped our group substantially in understanding the corresponding physics; to explain our experimental results on Vulcan and GEMINI laser facilities, and to propose new scheme for both ion acceleration and high-harmonic generation. A summary of the distinct elements of our work is shown below.

3.16.2   *Laser-driven ion acceleration*

Through a large number of 2D PIC simulations on the SCARF-INTEL and theoretical modelling, we have demonstrated that radiation pressure acceleration (RPA) is a very promising route to producing high-quality monoenergetic ion beams at currently achievable laser and target parameters. Depending on the foil density and thickness, the specific features of the hole-boring, light-sail and leaky light-sail regimes of RPA have been respectively simulated and analyzed. The key condition for stable RPA from thin foils by intense circularly polarized lasers has been identified. If this condition is satisfied the stable RPA regime can be extended from ultrahigh intensities $> 10^{22}$ Wcm^{-2} to currently accessible range 10^{20}-10^{21} Wcm^{-2}. The dependence of the RPA mechanism on laser polarization, intensity and on the target composition and areal density have also been studied with the help of various simulations. Our theoretical modelling and simulations have been verified and benchmarked by the experiments with GEMINI and VULCAN lasers

3.16.2.1 Identification of the key condition for radiation pressure acceleration (RPA)

We have identified the key condition for efficient and stable ion RPA from thin foils by CP laser pulses at moderate intensities through 2D PIC simulations. That is, the ion beam should remain accompanied with enough co-moving electrons to preserve a local bunching electrostatic field during the acceleration. With this key condition satisfied, the stable RPA regime can be extended from ultrahigh intensities $> 10^{22}$ Wcm^{-2} to currently accessible range $10^{20} - 10^{21}$ Wcm^{-2}, as shown in Figure 30, which shows the stable acceleration C^{6+} beam by laser pulse at intensity of 5×10^{20} Wcm^{-2}. This modelling is also directly relevant to experimental results, which are currently being prepared for publication.
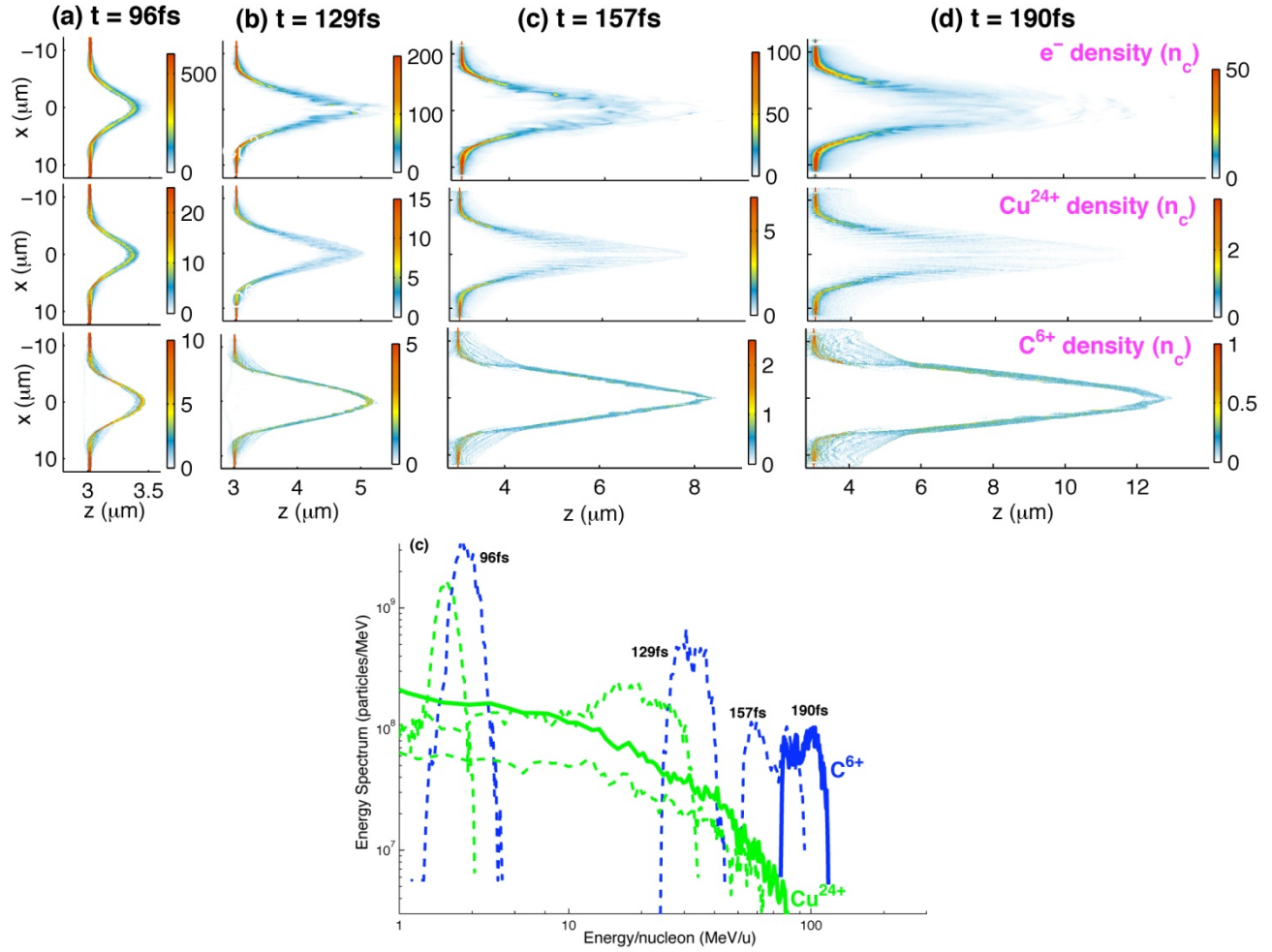
Figure 30: electron (e⁻), Cu²⁴⁺ and C⁶⁺ densities and their energy spectra for a 25nm Cu-C-mixed foil irradiated by lasers at intensity 5 x 10²⁰ Wcm⁻² at different times.

3.16.2.2 Hybrid ion acceleration regime

A novel regime is proposed where, employing linearly polarized laser pulses at moderate intensities, ions are dominantly accelerated from ultrathin foils by the laser radiation pressure, and have quasimonoenergetic spectra. In this regime, ions accelerated during the hole-boring process can quickly reach the foil rear surface and catch up with the ions accelerated by target normal sheath acceleration (TNSA). They join in a single bunch, which then undergoes a hybrid Light-sail/TNSA acceleration. Under an appropriate coupling condition between foil thickness, laser intensity and pulse duration, radiation pressure acceleration (RPA) can be dominant in this hybrid acceleration process at moderate intensities. Two-dimensional PIC simulations show that 1.26GeV quasimonoenergetic C6+ beams are obtained by linearly polarized laser pulses at intensities of 10²¹ Wcm⁻², as shown in Figure 31
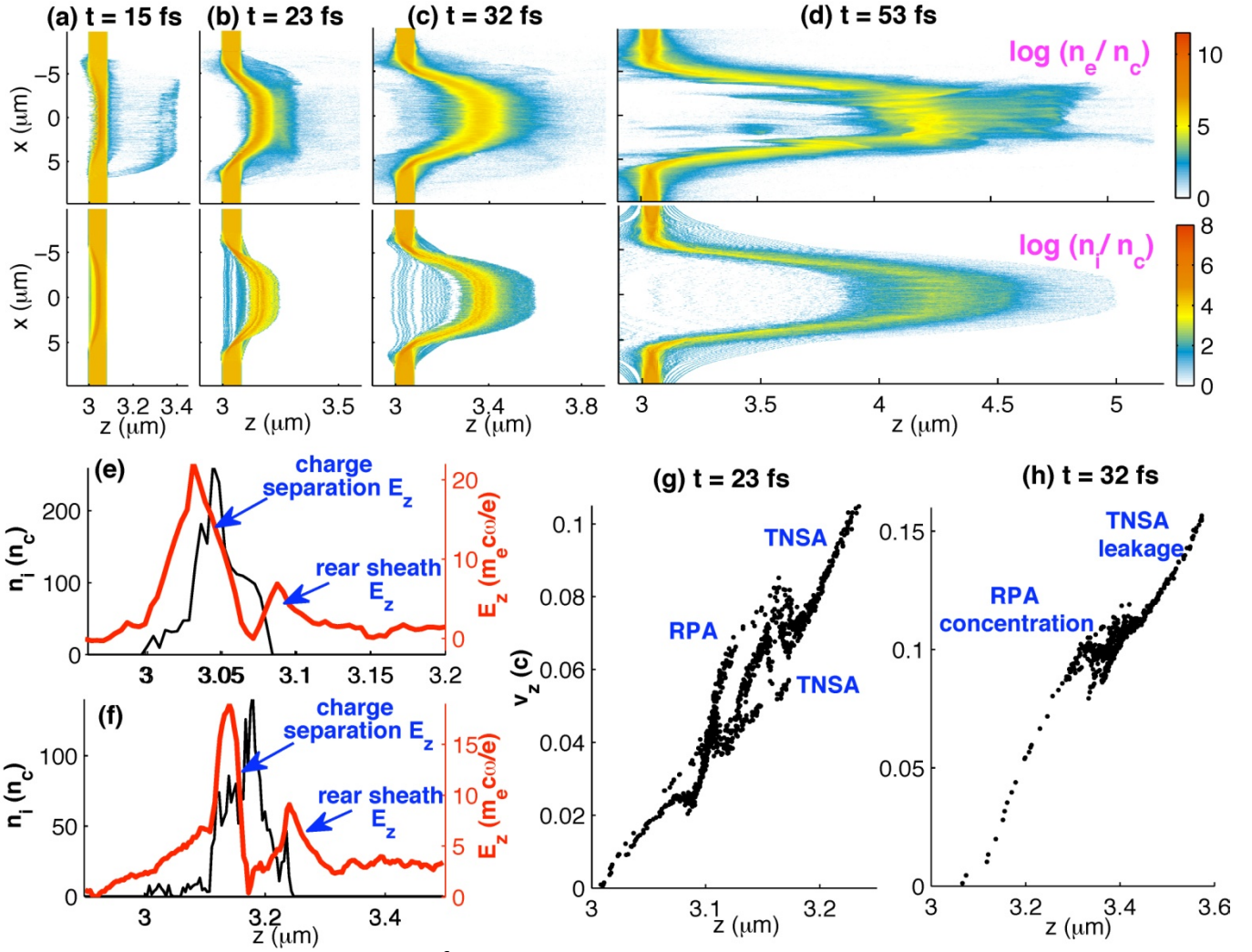
Figure 31: (a)-(d) Electron (ne) and ion (C^{6+}, ni) densities at respectively t = 15, 23, 32 and 53fs for a 80nm fully-inoized carbon foil irradiated by LP laser pulses at intensity I0 = 10^{21} W/cm^2 , wavelength λ = 1.0μm and duration τL = 20τ0 = 67fs, where the foil electron density is 600nc ;(e) and (f) the longitudinal profile of ni and electrostatic field Ez at t = 15 and 23fs, which shows ions are accelerated by a hybrid effect of the charge separation field and the rear sheath field, i.e., undergoing hybrid RPA-TNSA; (g) and (h) C^{6+} phase space distributions at t = 23 and 32fs, which show the typical characteristics of hybrid RPA-TNSA mechanism.

3.16.3 *Generation of relativistic electron mirror and high-harmonic generation:*

Recently, it was found in our experiments that ultrashort dense electron sheets can be generated from ultrathin foils by intense laser pulses approaching the blow-out regime. This sheet has extremely small thickness (nanometers), near-solid density and velocity close to *c*, are suitable for coherent reflection of a second counter-propagating pulse for frequency upshift, pulse compression and amplitude intensification. Our experiments have already observed the clear upshift signal. We have also run a number of simulations to explain these experiments. Figure 32 shows the clear upshift in spectrum of reflected probe pulse.

II. CP drive with/without LP probe

With no LP Probe

With LP Probe
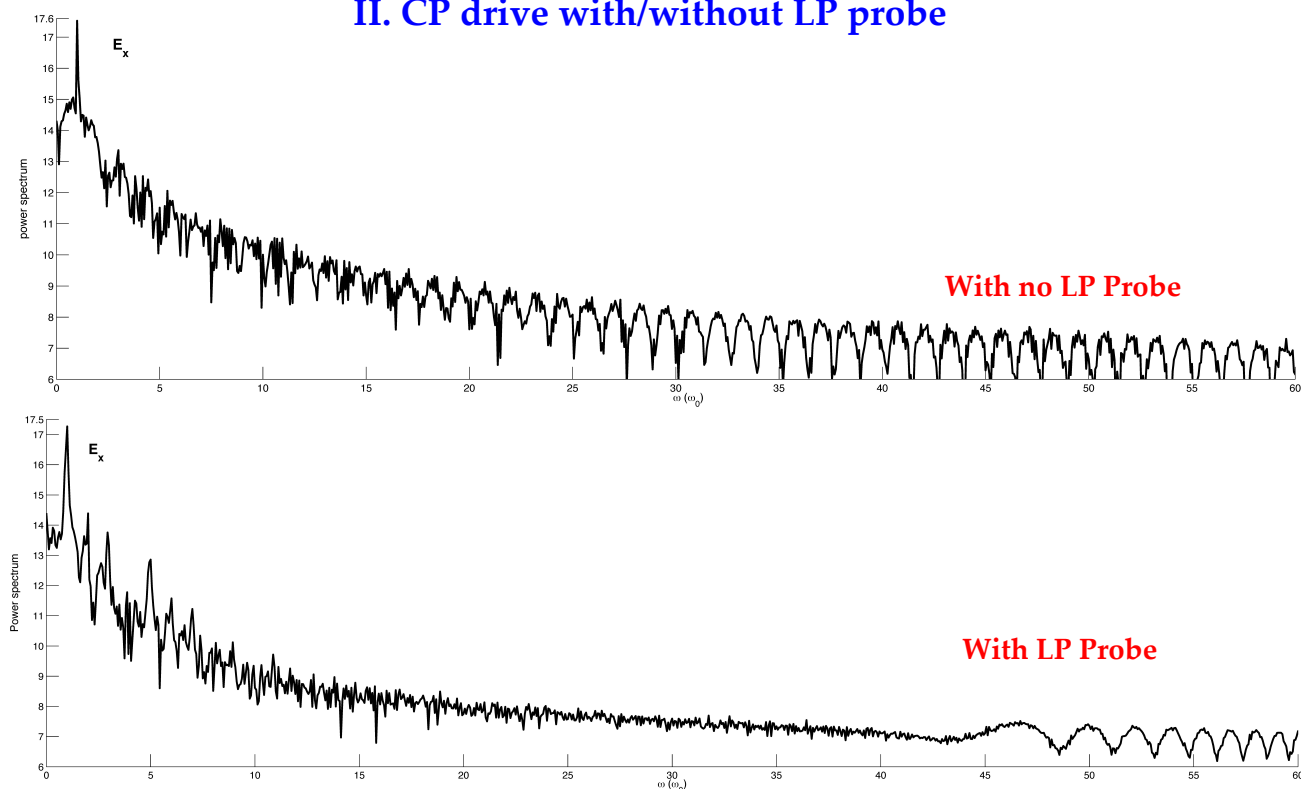
Figure 32: The frequency upshift when a probe pulse is reflected from a relativistic electron sheet generated by intense CP laser ultrathin foil interaction: the power spectrum of electric field with or without probe pulse.

All the above results will be submitted and/or published soon or have formed part of recent publications listed below. We are aiming for publication in high impact journals such as PRL/Nature Physics for our current work.

1.   APPENDIX : SCARF HARDWARE DETAILS

Host group	CPU type and frequency	Nodes	Cores /node	Total cores	Interconnect	Total memory
SCARF11	Intel X5660 @ 2.8GHz	32	12	384	QDR Infiniband	768GB
Lexicon-2/ SCARF10	Intel E5530 @ 2.40GHz	104	8	832	DDR Infiniband	2496 GB
IBIS/ SCARF09	Intel E5462 @ 2.80GHz	48	8	384	SDR Infiniband	768 GB
SCARF08	Intel E5430 @ 2.66GHz	46	8	368	SDR Infiniband	736 GB
Lexicon/ SCARF07	AMD Opteron 275 @ 2.2GHz	73	4	292	GB Ethernet	584 GB
General/ SCARF06	AMD Opteron 285 @ 2.6GHz	50	4	200	Myrinet	400 GB
Grand Totals		353		2460		5752GB

2.   APPENDIX: INDEX OF FIGURES

3.   APPENDIX: PUBLICATIONS AND PRESENTATIONS

#	Reference	Department
1.	S.Tomić, A. Marti, E. Antolin, A. Luque, "On inhibiting Auger intraband Auger relaxation in InAs/GaAs quantum dot intermediate band solar cells," accepted in Applied Physics Letters (available on request)	Stanko Tomic, CSED
2.	S. Tomić and N. Vukmirović, "Symmetry breaking in multiband Hamiltonians for semiconductor quantum dots: the role of interfaces and higher energy bands," accepted in Journal of Applied Physics	Stanko Tomic, CSED
3.	L.Bernasconi, S. Tomić, M. Ferrero, M. Rerat, R. Orlando, R. Dovesi, N. M. Harrison, "First-principles optical response of semiconductors and oxides," Physical Review B Volume: 83 Issue: 19 Article Number: 195325 Published: MAY 31 2011	Stanko Tomic, CSED
4.	N.Prodanović, J. Radovanović, V. Milanović, S. Tomić, „Genetic Algorithm Optimization of InAs/AlInAs Quantum Well Based Up-converter for Si Sollar Cells," submitted to journal of Applied Physics (available on request)	Stanko Tomic, CSED
5.	I.J. Bush,S. Tomić, B.G. Searle, G. Mallia, C.L. Bailey, B. Montanari, L. Bernasconi and N. M. Harrison, "Parallel implementation of the ab initio CRYSTAL program: Electronic structure calculations for periodic systems," Proceedings of the Royal Society A (invited paper) Volume: 467 Issue: 2131 Pages: 2112-2126 Published: JUL 8 2011	Stanko Tomic, CSED
6.	M.F.Pereira Jr. and S. Tomić,, "Intersubband gain without inversion through dilute nitride band engineering", Applied Physics Letters 98, 061101 (2011)	Stanko Tomic, CSED
7.	L. Liborio, C. L. Bailey, G. Mallia, S. Tomić, and N. M. Harrison, "Chemistry of Defect Induced Photoluminescence in Chalcopyrites: The case of CuAlS2", Journal of Applied Physics 109, 023519 (2011)	Stanko Tomic, CSED
8.	S. Tomić , "Intermediate band solar cells: influence of band formation on dynamical processes in InAs/GaAs quantum dot arrays," Physical Review B 82, 195321 (2010)	Stanko Tomic, CSED
9.	C. L. Bailey, L. Liborio, G. Mallia, S. Tomić, and N. M. Harrison, "Defect Physics of CuGaS2", Physical Review B 81, 205214 (2010)	Stanko Tomic, CSED
10.	Bell AR & Tzoufras M (2011), Plasma Phys & Controlled Fusion 53 045010	Tony Bell, Oxford/CLF
11.	Bell AR, Schure KM & Reville B (2011), Mon Not R Astr Soc, in press.	Tony Bell, Oxford/CLF
12.	G. Graziano, J. Klimeš, A. Michaelides, and F. Fernandez-Alonso, in preparation	Gabriella Graziano, UCL/ISIS
13.	M. Krzystyniak and F. Fernandez-Alonso, "Ab Initio Nuclear Momentum Distributions in Lithium Hydride: Assessing Nonadiabatic Effects," Physical Review B 2011 vol. 83 134305 (2011). [doi:10.1103/PhysRevB.83.134305]	Felix Fernandez-Alonso (ISIS) and Matthew Krzystyniak (Nottingham Trent University)
14.	M. Krzystyniak, M. A. Adams, A. Lovell, N. T. Skipper, S. M. Bennington, J. Mayers, and F. Fernandez-Alonso, "Probing the Binding and Spatial Arrangement of Molecular Hydrogen in Porous Hosts via Neutron Compton Scattering," Faraday Discussions 151 171-197 (2011). [doi: 10.1039/C1FD00036E].	Felix Fernandez-Alonso (ISIS) and Matthew Krzystyniak (Nottingham Trent University)
15.	M. Krzystyniak et al., in preparation.	Felix Fernandez-Alonso (ISIS) and Matthew Krzystyniak (Nottingham Trent University)
16.	Presentation: "Molecular Hydrogen in Nanoporous Materials: Unveiling the Potential of Neutron Compton Scattering." M. Krzystyniak, M.A. Adams, A. Lovell, N.T. Skipper, S.M. Bennington, J. Mayers, and F. Fernandez-Alonso (presenter). Poster presented at the 5th European Conference on Neutron Scattering ECNS 2011, July 17-22nd 2011, Prague, Czech Republic.	Felix Fernandez-Alonso (ISIS) and Matthew Krzystyniak (Nottingham Trent University)
17.	Presentation: "Proton Mobility in the Solid Super-proton Conductor CsHSO4." M. Krzystyniak (presenter), S. Richards, and F. Fernandez-Alonso. Poster presented at the 5th European Conference on Neutron Scattering ECNS 2011, July 17-22nd 2011, Prague, Czech	Felix Fernandez-Alonso (ISIS) and Matthew Krzystyniak (Nottingham Trent University)

	Republic.	
18.	Presentation: "Hydrogen Research with Neutrons: Why and How." F. Fernandez-Alonso. Invited seminar presented at the School of Physical Sciences, Nottingham Trent University, June 14th 2011, Nottingham, United Kingdom.	Felix Fernandez-Alonso (ISIS) and Matthew Krzystyniak (Nottingham Trent University)
19.	"Probing the Binding and Spatial Arrangement of Molecular Hydrogen in Porous Hosts via Neutron Compton Scattering." M. Krzystyniak, M.A. Adams, A. Lovell, N.T. Skipper, S.M. Bennington, and J. Mayers and F. Fernandez-Alonso (presenter). Talk presented at Faraday Discussion 151 – Hydrogen Storage Materials, April 18-20th 2011, Rutherford Appleton Laboratory, Didcot, United Kingdom.	Felix Fernandez-Alonso (ISIS) and Matthew Krzystyniak (Nottingham Trent University)
20.	Presentation:"Hydrogen Research with Neutrons: From Protonics to Gas Storage." F. Fernandez-Alonso. Invited seminar presented at the Department of Chemistry Seminar Series, University of Sussex, Oct 27th 2010, Brighton, United Kingdom.	Felix Fernandez-Alonso (ISIS) and Matthew Krzystyniak (Nottingham Trent University)
21.	Presentation:"How Quantum Mechanics Limits the Uptake of Molecular Hydrogen by Carbon-based Nanostructures." F. Fernandez-Alonso. Invited talk at the XV International Workshop on Quantum Atomic and Molecular Tunnelling in Solids and Other Condensed Phases, Sep 5-9th 2010, Darmstadt, Germany.	Felix Fernandez-Alonso (ISIS) and Matthew Krzystyniak (Nottingham Trent University)
22.	"Complete assignment of the vibrational modes of C60 by inelastic neutron scattering spectroscopy and periodic-DFT", S.F. Parker, S.M. Bennington, J.W. Taylor, H. Herman, I. Silverwood, P. Albers and K. Refson, Phys. Chem. Chem. Phys., 13 (2011) 7789 – 7804. [doi:10.1039/C0CP02956D]	Stewart Parker (ISIS)
23.	"Assignment of the vibrational spectra of lithium hydroxide monohydrate, LiOH.H2O", S.F. Parker, K. Refson, R.I. Bewley and G. Dent, J. Chem. Phys., 134 (2011) 084503. [doi: 10.1063/1.3553812]	Stewart Parker (ISIS)
24.	*The atomistic structure of a micelle in solution determined by wide Q-range neutron diffraction* Rowan Hargreaves, Daniel T Bowron and Karen Edler, **JACS** ,2011, Just accepted, **DOI:**10.1021/ja205804k	Rowan Hargreaves (ISIS)
25.	Eblagon KM, Tam K, Yu KMK, Zhao SL, Gong XQ, He HY, Ye L, Wang LC, Ramirez-Cuesta AJ, Tsang SC. Study of Catalytic Sites on Ruthenium For Hydrogenation of N-ethylcarbazole: Implications of Hydrogen Storage via Reversible Catalytic Hydrogenation. Journal of Physical Chemistry C 2010;114(21):9720-9730.	Timmy Ramirez-Cuesta (ISIS)
26.	Mulder FM, Assfour B, Huot J, Dingemans TJ, Wagemaker M, Ramirez-Cuesta AJ. Hydrogen in the Metal-Organic Framework Cr MIL-53. Journal of Physical Chemistry C 2010;114(23):10648-10655.	Timmy Ramirez-Cuesta (ISIS)
27.	Remhof A, Gremaud R, Buchter F, Lodziana Z, Embs JP, Ramirez-Cuesta TAJ, Borgschulte A, Zuttel A. Hydrogen Dynamics in Lightweight Tetrahydroborates. Zeitschrift Fur Physikalische Chemie-International Journal of Research in Physical Chemistry & Chemical Physics 2010;224(1-2):263-278.	Timmy Ramirez-Cuesta (ISIS)
28.	Seel AG, Sartbaeva A, Ramirez-Cuesta AJ, Edwards PP. Inelastic neutron scattering of Na-zeolite A with in situ ammoniation: an examination of initial coordination. Physical Chemistry Chemical Physics 2010;12(33):9661-9666.	Timmy Ramirez-Cuesta (ISIS)
29.	A. Borgschulte, R. Gremaud, A. J. Ramirez-Cuesta, K. Refson, A. Züttel. Evidence for Hydrogen Transport in Deuterated LiBH4 from Raman-scattering Measurements and First-principles Calculations. Advances in Science and Technology Vol. 72 (2010) pp 150-157	Timmy Ramirez-Cuesta (ISIS)
30.	Eblagon KM, Rentsch D, Friedrichs O, Remhof A, Zuettel A, Ramirez-Cuesta A, Tsang SC. Hydrogenation of 9-ethylcarbazole as a prototype of a liquid hydrogen carrier. International Journal of Hydrogen Energy 2010 Oct;35(20):11609-116211.	Timmy Ramirez-Cuesta (ISIS)
31.	Sartbaeva A, Wells S, Sommariva M, Lodge M, Jones M, Ramirez-Cuesta A, Li G, Edwards P. Formation of Crystalline Sodium Hydride Nanoparticles Encapsulated Within an Amorphous Framework. Journal of Cluster Science 2010 Sep;21(3):543-549.	Timmy Ramirez-Cuesta (ISIS)
32.	A Borgschulte, R Gremaud, F Buchter, Z Lodziana, A Zuttel, A Ramirez, Molecular Vibrations as the Origin of Solid State Effects in Borohydrides Proc. 2010 Materials Research Society (MRS), 2009, Mater. Res. Soc. Symp. Proc. Vol. 1216 © 2010 Materials Research Society. 1216-W07-09	Timmy Ramirez-Cuesta (ISIS)
33.	Milva Celli, Daniele Colognesi, Alessandra Giannasi, Lorenzo Ulivi, Marco Zoppi, Victoria Garcia Sakai, Aníbal Javier Ramírez-Cuesta, 'Simple and Binary Hydrogen Clathrate Hydrates: Synthesis and Microscopic Characterization through Neutron and Raman Scattering' Advances in Science and Technology, 72, 196, 2010.	Timmy Ramirez-Cuesta (ISIS)
34.	Daniele Colognesi, Antonino Pietropaolo, Aníbal Javier Ramírez-Cuesta, Michele Catti, Angelo Claudio Nale, Marco Zoppi, 'Proton Vibrations in Lithium Imide and Amide Studied through Incoherent Inelastic Neutron Scattering', Advances in Science and Technology, 72, 158, 2010.	Timmy Ramirez-Cuesta (ISIS)
35.	A. Giannasi, D. Colognesi, L. Ulivi, M. Zoppi, A. J. Ramirez-Cuesta, E. G. Bardají, E. Roehm,	Timmy Ramirez-Cuesta (ISIS)

	M. Fichtner 'High Resolution Raman and Neutron Investigation of Mg(BH4)2 in an Extensive Temperature Range' The Journal of Physical Chemistry A 2010 114 (8), 2788-2793	
36.	Borgschulte, A.; Gremaud, R.; Zuttel, A.; Martelli, P.; Remhof, A.; Ramirez-Cuesta, A.; Refson, K.; Bardaji, E.; Lohstroh, W.; Fichtner, M.; Hagemann, H.; Ernst, M., Experimental evidence of librational vibrations determining the stability of calcium borohydride. Physical Review B 2011, 83 (2).	Timmy Ramirez-Cuesta (ISIS)
37.	Ryan, K. R.; Ramirez-Cuesta, A. J.; Refson, K.; Jones, M. O.; Edwards, P. P.; David, W. I. F., A combined experimental inelastic neutron scattering, Raman and ab initio lattice dynamics study of alpha-lithium amidoborane. Physical Chemistry Chemical Physics 2011, 13 (26), 12249-12253.	Timmy Ramirez-Cuesta (ISIS)
38.	D. Colognesi, A. Giannasi, L. Ulivi, M. Zoppi, A. J. Ramirez-Cuesta, A. Roth, M. Fichtner Raman and Inelastic Neutron Scattering Study on a Melt-Infiltrated Composite of NaAlH4 and Nanoporous Carbon The Journal of Physical Chemistry A 2011 115 (26), 7503-7510	Timmy Ramirez-Cuesta (ISIS)
39.	Toyoto Sato, A. J. (Timmy) Ramirez-Cuesta, Kazutaka Ikeda, Shin-ichi Orimo, Kazuyoshi Yamada, Vibrational Properties of CaAlH5 and α-AlH3 with Different AlH6 Networks Studied by Inelastic Neutron Scattering, Inorganic Chemistry 2011 50 (17), 8007-801	Timmy Ramirez-Cuesta (ISIS)
40.	A. Borgschulte, E. Callini, B. Probst, A. Jain, S. Kato, O. Friedrichs, A. Remhof, M. Bielmann, A. J. Ramirez-Cuesta, A. Zuttel, Impurity Gas Analysis of the Decomposition of Complex Hydrides, The Journal of Physical Chemistry C 2011 115 (34), 17220-17226	Timmy Ramirez-Cuesta (ISIS)
41.	Presentation: "Dynamics of some porous materials using inelastic Neutron scattering spectra" 5th International FEZA Conference, (3-7 July 2011) Valencia, Spain.	Timmy Ramirez-Cuesta (ISIS)
42.	Presentation: "Studying hydrogen storage using computers and neutron scattering" Materials modeling Laboratory, Materials Sciences Department, Oxford. 4th February 2011.	Timmy Ramirez-Cuesta (ISIS)
43.	Presentation: "Investigation into the reversibility of TiCl4 doped NaAlH4 using inelastic neutron scattering" Symposium on Advances in Chemistry and Materials for Hydrogen Storage, Pacifichem Conference, Honolulu, Hawaii, 14-18 December 2010, invited talk.	Timmy Ramirez-Cuesta (ISIS)
44.	Presentation: "Using neutrons and computers to understand the hydrogen storage problem," seminar at EMPA, 22-23 November 2010, invited talk.	Timmy Ramirez-Cuesta (ISIS)
45.	Presentation: "The Power of Inelastic Neutron Scattering: Vibrational Spectroscopy of hydrogen - applications to catalysis"Neutrons for Catalysis: A Workshop on Neutron Scattering Techniques for Studies in Catalysis Oak Ridge National Laboratory (September 16-17, 2010), invited talk.	Timmy Ramirez-Cuesta (ISIS)
46.	Presentation: 'Mobility and dynamics in the complex hydrides LiAlH4 and LiBH4', invited talk, Faraday Discussion 151: Hydrogen Storage Materials, Rutherford Lab, Didcot, UK, 18. - 20.04.2011	Timmy Ramirez-Cuesta (ISIS) Andreas Borgschulte (EMPA)
47.	Presentation: 'Hydrogen sorption kinetics, reaction dynamics, and spectroscopy', invited talk, Workshop "X-Rays and Neutrons in Energy-Releated Materials Science", Département de Chimie Physique, Université Genève, Switzerland, 29. 03. 201	Timmy Ramirez-Cuesta (ISIS) Andreas Borgschulte (EMPA)
48.	Presentation: 'Structure and dynamics of complex hydrides', invited talk, ESRF user meeting 2011, Grenoble, France, 09. 02. 2011	Timmy Ramirez-Cuesta (ISIS) Andreas Borgschulte (EMPA)
49.	Presentation: 'Building Blocks of the Pseudo-Ternary System LiBH4-LiNH2-LiI', talk, 5th Int. Symosium Hydrogen & Energy, Seminarhotel Stoos, Stoos, Switerland, 23. - 28.01.2011	Timmy Ramirez-Cuesta (ISIS) Andreas Borgschulte (EMPA)
50.	Title: Conditions for efficient and stable ion acceleration by moderate circularly polarized laser pulses at intensities of 10(20) W/cm(2) Author(s): Qiao B.; Zepf M.; Gibbon P.; et al. PHYSICS OF PLASMAS Volume: 18 Issue: 4 Article Number: 043102 DOI: 10.1063/1.3577573 Published: APR 2011	Bin Qiao (QUB) David Neely (STFC)
51.	Ion source development and radiobiology applications within the LIBRA project Author(s): Borghesi M.; Kar S.; Prasad R.; et al. Editor(s): Leemans WP; Esarey E; Hooker SM; et al. Conference: Conference on Laser Acceleration of Electrons, Protons, and Ions and Medical Applications of Laser-Generated Secondary Sources of Radiation and Particles Location: Prague, CZECH REPUBLIC Date: APR 18-20, 2011 Sponsor(s): SPIE Source: LASER ACCELERATION OF ELECTRONS, PROTONS, AND IONS AND MEDICAL APPLICATIONS OF LASER-GENERATED SECONDARY SOURCES OF RADIATION AND PARTICLES Book Series: Proceedings of SPIE-The International Society for Optical Engineering Volume: 8079 Article Number: 80791E DOI: 10.1117/12.888262 Published: 2011	Bin Qiao (QUB) David Neely (STFC)
52.	Key conditions for stable ion radiation pressure acceleration by circularly polarized laser pulses Author(s): Qiao B.; Zepf M.; Gibbon P.; et al. Editor(s): Leemans WP; Esarey E; Hooker SM; et al. Conference: Conference on Laser Acceleration of Electrons, Protons, and Ions and Medical Applications of Laser-Generated Secondary Sources of Radiation and Particles Location: Prague, CZECH REPUBLIC Date: APR 18-20, 2011 Sponsor(s): SPIE Source: LASER ACCELERATION OF ELECTRONS, PROTONS, AND IONS AND MEDICAL APPLICATIONS OF LASER-GENERATED SECONDARY SOURCES OF RADIATION AND	Bin Qiao (QUB) David Neely (STFC)

	PARTICLES Book Series: Proceedings of SPIE-The International Society for Optical Engineering Volume: 8079 Article Number: 80790Q DOI: 10.1117/12.890018 Published: 2011	
53.	Generation and optimization of electron currents along the walls of a conical target for fast ignition Author(s): Micheau S.; Debayle A.; d'Humieres E.; et al. Source: PHYSICS OF PLASMAS Volume: 17 Issue: 12 Article Number: 122703 DOI: 10.1063/1.3521571 Published: DEC 2010	Bin Qiao (QUB) David Neely (STFC)
54.	Radiation-pressure acceleration of ion beams from nanofoil targets: the leaky light-sail regime. Author(s): Qiao B; Zepf M; Borghesi M; et al. Source: Physical R eview letters Volume: 105 Issue: 15 Pages: 155002 Published: 2010-Oct-8	Bin Qiao (QUB) David Neely (STFC)
55.	Radiation-Pressure Acceleration of Ion Beams from Nanofoil Targets: The Leaky Light-Sail Regime Author(s): Qiao B.; Zepf M.; Borghesi M.; et al. Source: PHYSICAL REVIEW LETTERS Volume: 105 Issue: 15 Article Number: 155002 DOI: 10.1103/PhysRevLett.105.155002 Published: OCT 4 2010	Bin Qiao (QUB) David Neely (STFC)

4.   APPENDIX: SCARF QUEUE USAGE 2010-11

Key:

- **Red - number of jobs running**
- **Green – number of jobs pending**
- **Blue – number of jobs gather CPUs so that they can run (large parallel jobs)**
- **Black - total number of Jobs (sum of Red, Green, Blue)**

4.1   General SCARF Queue

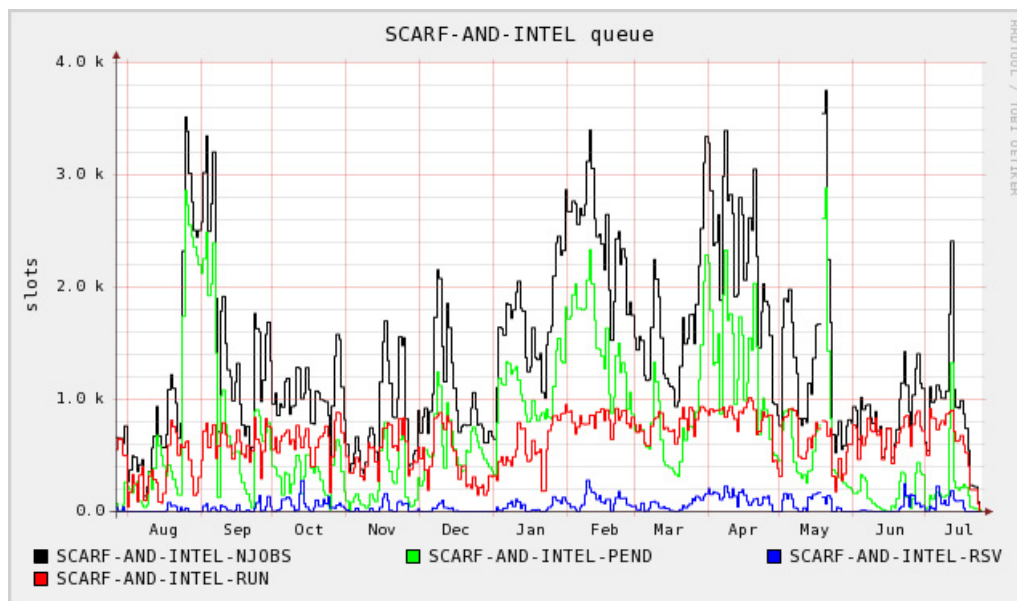Open to all SCARF Users with a capacity of ~1200 CPU cores

Figure 33: SCARF Queue Usage

The graph for the SCARF queue (and thus the combined SCARF/INTEL graph) shows consistently pending jobs for most of the year, which demonstrates that there is not sufficient capacity. This should be addressed by the next hardware procurement.

4.2   SCARF-Lexicon[1-2] Queues

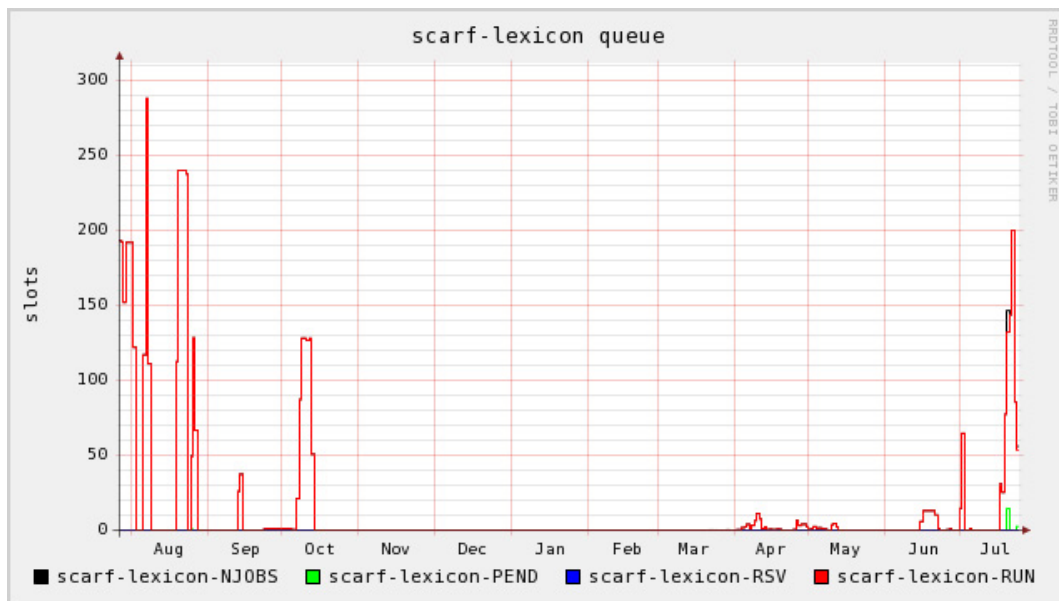These queues are primarily for CLF use with a capacity of 292 and 544 CPU cores for SCARF Lexicon 1 & 2 respectively.

Figure 34: SCARF-Lexicon Usage

The graph for the SCARF-LEXICON queue shows peaky but significant usage, though this has dropped somewhat since the purchase of SCARF-LEXICON-2.
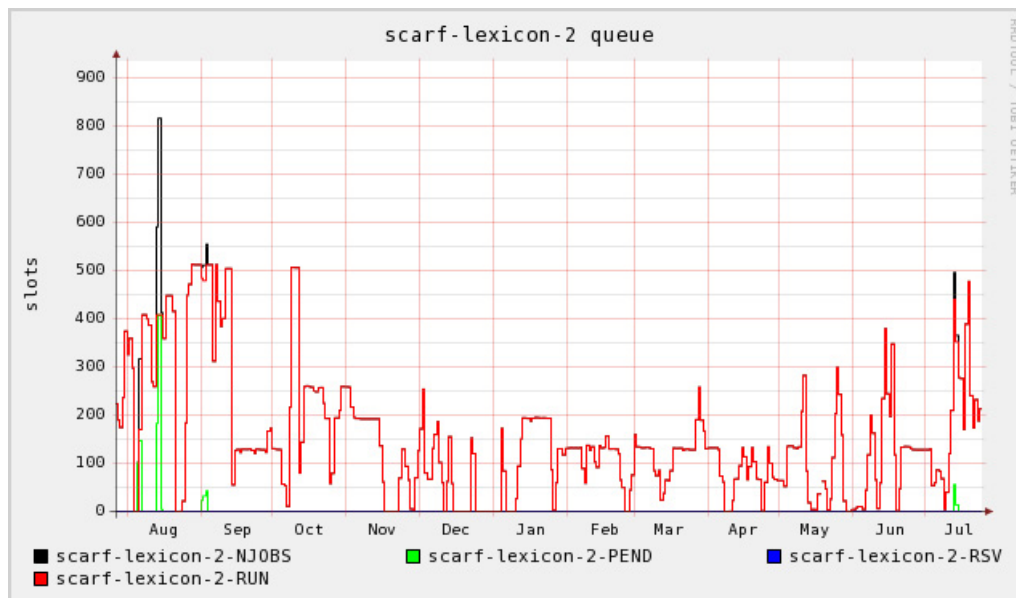

Figure 35: SCARF Lexicon-2 Usage

SCARF-LEXICON-2 shows steadily increasing usage towards the maximum capacity, which is excellent given that there have been some initial issues with the hardware which have reduced the amount of time available to the group.

4.3   SCARF-IBIS

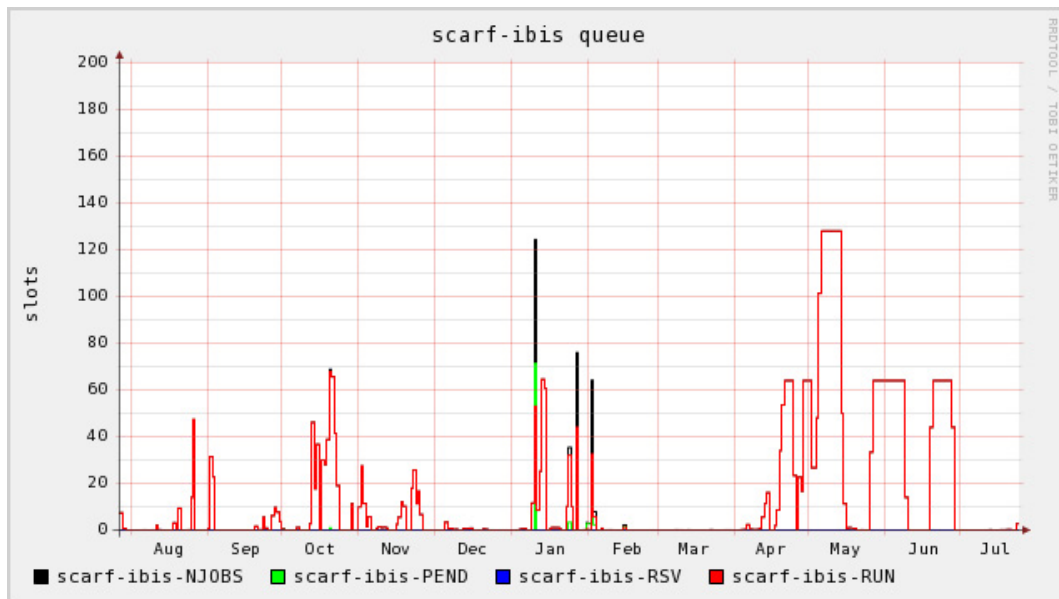SCARF-IBIS has a capacity of 144 CPU cores.

Figure 36: SCARF-IBIS Usage

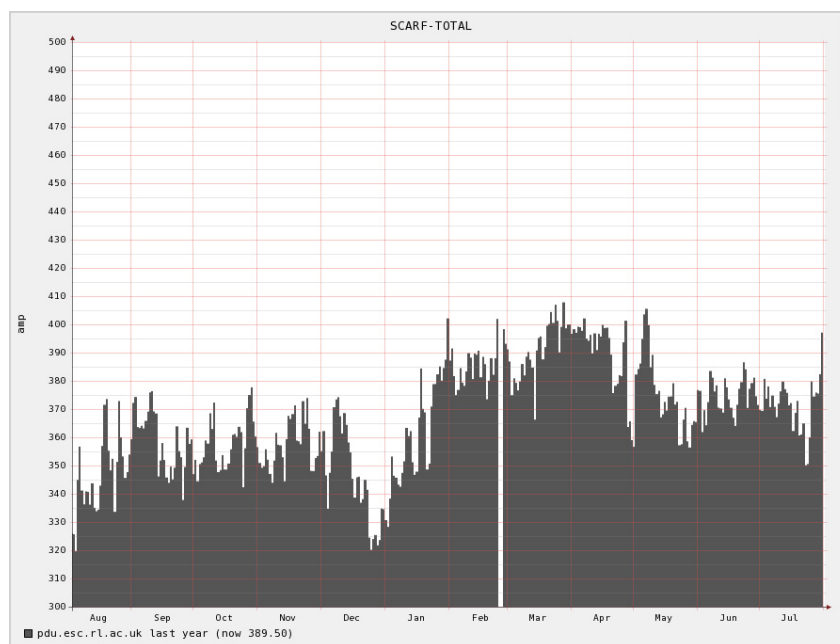## 4.4   SCARF Total Power draw (amps)

Figure 37: SCARF Power Usage

The approximate average power draw of the SCARF cluster (including Lexicon) is about 380 amp or 91kW/hr. This excludes the power needed to cool, pump and move cold air. The efficiency of SCARF in terms in Gflops/W is giving in the table below.

Year Purchased	Gflops/W
2006	0.07
2007	0.09
2008	0.21
2009	0.29
2010	0.32
2011	0.48

Figure 38: GFlops/W for SCARF generations of equipment

From the above table it is clear that the Gflops/W achieved increase per generation of the SCARF equipment. This supports the continual refresh rate of SCARF hardware rather than a big bang approach.

5.   APPENDIX – SCARF DEVELOPMENTS

It has been a busy year for the SCARF service. Users' will have noticed most impact with the additional of capacity, upgrades to applications and a change in access to SCARF. However, a lot of effort goes into improving the management of SCARF. SCARF is also part of NGS which allows users to use grid technology to access a larger pool of resources.

5.1   Technical Developments

- Deployment of Red Hat 5/LSF 8/MPI 8
  The most significant development has been the rollout of a new operating environment to the cluster nodes. As this was such a significant change, the initial plan to install the entire cluster in one step was revised to one that phased in the deployment, allowing users concurrent access to both the old and new environments. This was done to allow compilation and testing of codes in the new environment, while still allowing useful work to be run via the old environment. MPI8 is a merging of ScaliMPI we used under RHEL4 and HP-MPI and provides the speed and fault tolerance of ScaliMPI with the flexibility and improved commercial support of HP-MPI. It provides a full MPI2 / MPI I/O implementation which several scientific codes are now requiring. ScaliMPI is no longer supported.
  This was a big change as all applications will need to be recompiled, installed and tested.
  Initial deployment was completed by the end of July 2011.
- Installation of Scarf 11 nodes
  In May, the 32 hosts that comprised the SCARF 2011 hardware purchase were released for use. These nodes are the first 12 core systems in SCARF, providing 384 cores in total and are also the first with Quad Data Rate Infiniband.
  Despite initial technical difficulties these were resolved in May 2011 and the new capacity has been available since then with no issues.
- Migration to new Applications server
  The file server that provides most user applications developed significant hardware problems and was replaced with a newer system.

5.2   Application Stack

Applications available under the new RedHat 5/LSF 8/MPI 8 environment are in the table below:

Application	Area	Version
Gaussian	Computational Chemistry	g09_B01
ABAQUS	Engineering	6.10-2
CASTEP	Computational Chemistry	5.5.2
ORBIT		1.0 ,2.0, 3.0
xmgrace		5.1.21
DL_POLY	Computational Chemistry	2.20 , 3.09, 4.02
IDL		8.1
Intel compiler	Fortran, C, C++ compilers and Maths libraries	12.0
PGI compilers	Fortran, C, C++ compilers and Maths libraries	11.6

Figure 39: SCARF Application Stack

5.3   Staff Movements

There was a change of management of the SCARF service, Duncan Tooke left STFC in October 2010 and Jon Churchill stepped in as the temporary manager. After a recruitment exercise Derek Ross started in May 2011 and is now the primary SCARF Manager with Jonathan Churchill looking after applications.